FEATURE ARTICLE

The Fermi energy as common parameter to describe charge compensation mechanisms: A path to Fermi level engineering of oxide electroceramics

Andreas Klein[1] · Karsten Albe[1] · Nicole Bein[1] · Oliver Clemens[2] · Kim Alexander Creutz[1] · Paul Erhart[3] · Markus Frericks[1] · Elaheh Ghorbani[1] · Jan Philipp Hofmann[1] · Binxiang Huang[1] · Bernhard Kaiser[1] · Ute Kolb[4,5] · Jurij Koruza[6] · Christian Kübel[7,8] · Katharina N. S. Lohaus[1] · Jürgen Rödel[7] · Jochen Rohrer[1] · Wolfgang Rheinheimer[9] · Roger A. De Souza[10] · Verena Streibel[11] · Anke Weidenkaff[7,12] · Marc Widenmeyer[7] · Bai-Xiang Xu[1] · Hongbin Zhang[1]

Abstract

Chemical substitution, which can be iso- or heterovalent, is the primary strategy to tailor material properties. There are various ways how a material can react to substitution. Isovalent substitution changes the density of states while heterovalent substitution, i.e. doping, can induce electronic compensation, ionic compensation, valence changes of cations or anions, or result in the segregation or neutralization of the dopant. While all these can, in principle, occur simultaneously, it is often desirable to select a certain mechanism in order to determine material properties. Being able to predict and control the individual compensation mechanism should therefore be a key target of materials science. This contribution outlines the perspective that this could be achieved by taking the Fermi energy as a common descriptor for the different compensation mechanisms. This generalization becomes possible since the formation enthalpies of the defects involved in the various compensation mechanisms do all depend on the Fermi energy. In order to control material properties, it is then necessary to adjust the formation enthalpies and charge transition levels of the involved defects. Understanding how these depend on material composition will open up a new path for the design of materials by Fermi level engineering.

✉ Andreas Klein
aklein@esm.tu-darmstadt.de

[1] Institute of Materials Science, Technical University of Darmstadt, Otto-Berndt-Straße 3, Darmstadt 64287, Germany

[2] Institute of Materials Science, University of Stuttgart, Heisenbergstr. 3, Stuttgart 70569, Germany

[3] Department of Physics, Chalmers University of Technology, Gothenburg 41296, Sweden

[4] Institute of Applied Geosciences, Technical University of Darmstadt, Schnittspahnstraße 9, Darmstadt 64287, Germany

[5] Department of Chemistry, Johannes Gutenberg University Mainz, Jakob-Welder-Weg 11, Mainz 55128, Germany

[6] Institute for Chemistry and Technology of Materials, Graz University of Technology, Stremayrgasse 9, Graz 8010, Austria

[7] Institute of Materials Science, Technical University of Darmstadt, Peter-Grünberg-Straße 2, Darmstadt 64287, Germany

[8] Institute of Nanotechnology, Karlsruhe Institute of Technology, Hermann-von-Helmholtz-Platz 1, Eggenstein-Leopoldshafen 76344, Germany

[9] Institute of Energy and Climate Research IEK-1, Jülich Research Center, Wilhelm-Johnen-Straße, Jülich 52428, Germany

[10] Institute of Physical Chemistry, RWTH Aachen University, Landoltweg 2, Aachen 52056, Germany

[11] Walter-Schottky-Institut, Technische Universität München, Am Coulombwall 4, Garching 85748, Germany

[12] Fraunhofer Research Institution for Materials Recycling and Resource Strategies IWKS, Aschaffenburger Str. 121, Hanau 63457, Germany

1 Introduction

Multinary oxide electroceramics provide a vast range of functional properties depending on their composition, structure, and defect properties. They have experienced a tremendous development in the last fifty years and are of increasing importance in many key technologies, including communication, energy conversion and storage, electronics and automation [1–3]. The class of oxide electroceramics comprises dielectrics for capacitors [4, 5], materials for fuel cells and gas permeation membranes [6], as well as piezo- and ferroelectrics for non-volatile memories [7], actuators, and transducers [8]. Electroceramic oxides are also key materials for photocatalysis and widely studied for replacing electrode and solid electrolyte materials for rechargeable batteries [9], and magnetic or memristive materials for data storage and neuromorphic computation [10]. Semiconducting oxides are key sensor materials for environmental monitoring, transparent electrodes in solar cells and displays, and outperform amorphous silicon in thin film transistors [11]. These and other applications require materials with tailored properties, which are governed by their bulk, interfacial, and microstructural features.

Driven by the need for novel and improved functionalities, reduced use of hazardous and critical raw materials, miniaturization and costs, the field of electroceramics is expected to further grow rapidly, requiring materials to fulfill a set of requirements that might be mutually exclusive. Oxygen transport membranes require, for example, both high ionic and electronic conductivities together with fast surface exchange reactions and resistance towards carbonate formation. Piezoceramics, as another example, must feature certain piezoelectric figures-of-merit but also fulfill mandates for temperature- and frequency-dependent losses. In order to cope with such challenges, doping and co-doping are often used in an extensive trial-and-error approach as there is still a lack of understanding of the interplay of structural, chemical and electronic effects. The same holds for grain boundaries and surfaces, for which structural distortions and variations in chemical composition must also be considered.

In the last decades, research on functional ceramics has brought tremendous progress for a better understanding of structure-property relations through advanced characterization methods, including spectroscopy and microscopy, as well as high-fidelity electronic structure calculations. Nevertheless, scientific and experimental progress is often still the result of serendipity. Researchers experience that subtle changes in composition and/or processing can result in a substantial variation of properties, whereby tiny differences in the impurity content of the starting materials or processing conditions strongly affect reproducibility. The ability to predict properties of materials with given compositions and processing parameters, which is possible with modern simulation tools in semiconductor technology (TCAD: Technology Computer Aided Design), is not yet available for electroceramics.

The main strategy to adjust properties of functional ceramics is the subtle and controlled variation of the chemical composition by substitution. While isovalent substitution or the formation of solid solutions is electrically neutral, heterovalent substitution (doping) introduces additional charged defects.[1] Doping can result in different properties, which are primarily determined by how the charges introduced by the dopant species are compensated in the material. In semiconductors, dopants are mostly *electronically compensated* by electrons and electron-holes (holes), which are highly mobile electronic charge carriers [12]. Doping in oxides is often *ionically compensated* by introduction of ionic defects, such as vacancies or interstitials, which can result in ion conducting materials to be used in fuel cells, batteries or membranes [13]. The compensation by ionic defects is also used to explain the variation of properties of soft- (donor) or hard- (acceptor) doped piezoelectrics [14]. For higher doping levels, the solubility limit may be exceeded resulting in the *segregation* of dopants to grain boundaries, surfaces, and heterointerfaces or leading to the formation of secondary phases. Such effects are, for example, intentionally utilized in ZnO varistor ceramics or $BaTiO_3$ conductors (PTCR: positive temperature coefficient resistors) [15, 16]. Furthermore, charge compensation can occur via *valence changes* of constituents, being the origin of unique magnetic properties as the basis for memory and sensor applications [10, 17–19]. The variety of charge compensation mechanisms, resulting material properties, and applications based on the different compensation mechanisms are summarized in Fig. 1.

Charge compensation mechanisms are well understood for many materials and used to iteratively optimize their properties. However, literature does not provide a description of all different mechanisms on a common basis. To this end, the electrochemical potential of the electrons, which is commonly referred to as the Fermi energy, can be seen as hidden variable in the development and engineering of electroceramics. It is a precisely defined thermodynamic quantity in solids. At finite temperatures, an electronic state, having an energy equal to the Fermi energy, has a 50 % probability of being occupied. The Fermi energy does not necessarily coincide with an existing energy level that can be occupied (in an insulator, for example, the Fermi level lies in the band gap), nor does it require the existence

---

[1] To distinguish between substitution requiring charge compensation or not, the term "doping" is exclusively used for heterovalent substitution in this contribution.
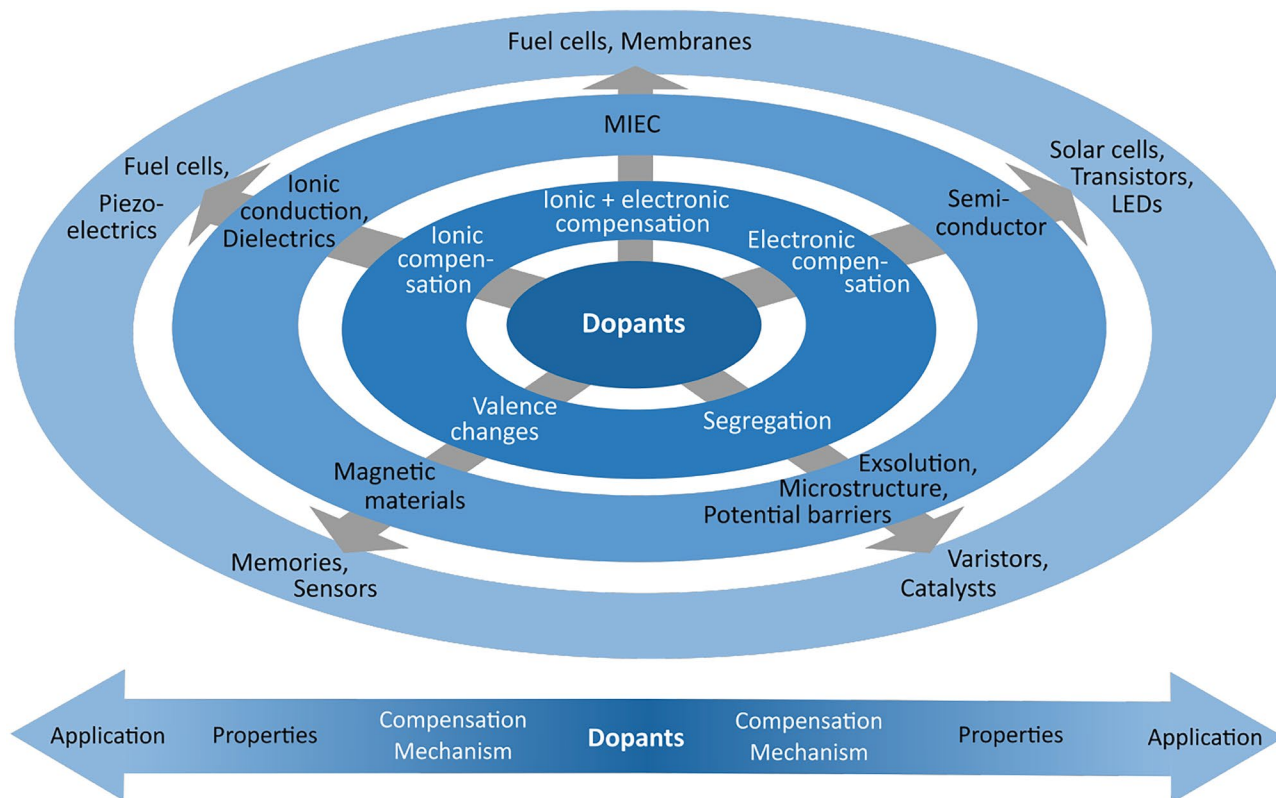
Fig. 1 The charges introduced by doping can be compensated by different mechanisms, resulting in a wide variation of material properties enabling a plethora of different applications

of a band structure with extended electronic states. It has the potential to serve as key descriptor for a wide variety of properties in the context of a knowledge-based materials design. The fundamental origin of this is the mutual relation between defect concentrations and the Fermi energy to establish charge neutrality. While it is clear that the Fermi energy is determined by the defect concentrations and their defect energy levels, it is less common knowledge that the defect concentrations are also intimately connected to the Fermi energy.

In this contribution, the Fermi energy is proposed as the key quantity for comparing charge compensation mechanisms. It provides a unique basis for predicting material properties of electroceramic oxides and is essential for the adjustment and improvement of manifold material properties. After some introductory remarks about defect properties and the Fermi energy in Section 2, the different charge compensation mechanisms and their relation to the Fermi energy will be described in Section 3. The tools of Fermi level engineering, that is how the charge compensation mechanisms can be manipulated in order to adjust material properties, will be outlined in Section 4. This includes the influence of the density of states, of the energy band alignment, and of the defect energy levels of dopants. The

article continuous with two short excursions on the impact of the Fermi energy on space charge regions at interfaces in Section 5 and on how the knowledge about the charge compensation mechanisms and the variation of the Fermi energy might eventually be utilized to select sample processing conditions in Section 6.

2 The Fermi energy and defect properties

2.1 The electron chemical potential and the Fermi energy

Electrons are Fermions with a spin $\frac{1}{2}$. The occupation of electronic states at energy E by electrons is thus given by the Fermi-Dirac distribution $f(E)$ [12]:

$$f(E) = \frac{1}{1 + \exp\left(\frac{E - \mu_e}{k_B T}\right)}. \tag{1}$$

where μ_e is the (electro)chemical potential of the electrons, k_B is Boltzmann's constant and T is the temperature. The course of the Fermi distribution function, $f(E)$, at different temperatures is illustrated in Fig. 2.
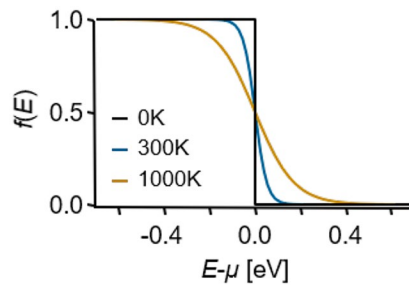
Fig. 2 The Fermi distribution function at different temperatures

At zero Kelvin, $f(E)$ is a step function. Therefore, all states below the Fermi energy are occupied and states above are empty. With increasing temperature, $f(E)$ broadens around μ by about $6\,k_\mathrm{B}T$. Thermodynamically, μ_e represents the reservoir from which electrons are drawn. At this point, the electron chemical potential is a "free" variable (in the thermodynamic sense). The Fermi energy, E_F, (note that it is not a potential) is in principle the value of μ_e at which *charge neutrality* is obtained. This couples all the quantities that depend on the electron chemical potential, including all defect concentrations as well as contributions associated with surfaces and interfaces (trap states, surface potentials). In thermodynamic equilibrium, one can therefore replace μ by E_F in Eq. 1, as it is commonly done in semiconductor textbooks [12]. In solid state physics textbooks (see, e.g., [20, 21]), the Fermi energy is usually derived as the highest occupied level of a free electron gas at zero Kelvin, which is given by

$$E_\mathrm{F} = \frac{\hbar^2}{2m}\left(3\pi^2 n\right)^{2/3} \tag{2}$$

where $\hbar$ is Planck's constant, m the mass of the electron, and n the concentration of the electrons, which is equal to the number of positively charged atoms. As the density of states in the free electron gas increases with $\sqrt{E}$, the energy level at which 50 % of the electronic states are occupied must reduce in energy upon an increase of temperature in order to leave the concentration of electrons unaltered. Sometimes the term *Fermi level* is then used for the temperature dependent quantity [21]. We will not distinguish between Fermi energy and Fermi level in this contribution.

2.2 Defects in materials

2.2.1 Defect concentrations and charge states

Defects in materials can be classified according to their dimension. There are three-dimensional (voids), two dimensional (interfaces, including grain boundaries and surfaces),

one-dimensional (dislocations), and zero-dimensional (point) defects. This contribution will cover only parts of the properties of defects: Thermodynamic properties of point defects will be outlined in Section 2.2, whereas Section 5 will elaborate on the relation between point defects and planar (two-dimensional) defects. The influence of strain will also not be covered. Regarding electronic properties, strain is known to modify the position and the dispersion of energy bands [22] but is also expected to affect defect formation energies and the charge transition levels of defects. Both will change defect concentrations and cannot be ignored. In the context of strain, the influence of temperature must be considered. Defect concentrations in oxides are typically established during synthesis, typically performed at very high temperatures, often $> 1000\,°C$. On the other hand, the impact of strain on material properties is typically discussed at operation temperatures, which are much lower. Strain develops largely during cooling and is eventually affected by microstructure and, in addition, by ferroelectric or electrochemical polarization. Revealing the relation between strain and defect proporties is beyond the scope of this contribution and has to be treated separately.

Point defects in a material are cation and anion vacancies (V_{cat}, V_{an}) and interstitials (Cat_i, An_i), antisite defects (Cat_{an}, An_{cat}), electrons in the conduction band (e), holes in the valence band (h, sometimes also referred to as electron-holes), and trapped electrons and holes. More details about trapped charges will be given in Section 3.3. All the above mentioned defects are referred to as *intrinsic defects* throughout this contribution. In addition to the intrinsic defects, *extrinsic defects* are induced by intentional substitution or unintentionally by impurities.

The mole fraction of an intrinsic defect species D in a material is given by:

$$[D] = \frac{N_D}{N_{D,0}} = \exp\left(-\frac{\Delta G_D}{k_\mathrm{B}T}\right) \tag{3}$$

where $N_{D,0}$ is the concentration of potential defect sites, e.g., the concentration of anions for anion vacancies. ΔG_D is the free formation energy of the defect. *The formation energies of intrinsic defects must be positive.* If not, the number of defects will be higher than the number of potential defect sites, resulting in a disintegration of the material. Consequently, the generation of defects raises the enthalpy, H, of the system. However, the free enthalpy of the system, $G = H - TS$ can be lowered by the generation of defects due to the increasing configurational entropy, S. Eventually, the minimum of G, is obtained if the concentration of defects corresponds to that given by Eq. 3 [13]. The free formation enthalpy of the defects contains all other entropy contributions, such as changes in vibrational entropy upon defect formation (see, e.g., [23]).
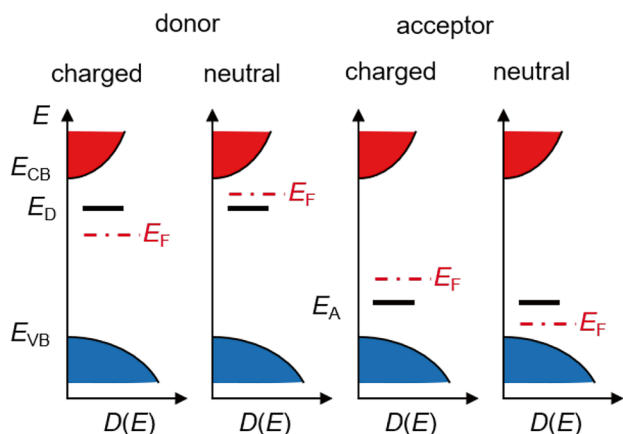
Fig. 3 Dependence of charge state of donors and acceptors with charge transition levels E_D and E_A on the Fermi energy E_F. The donor/acceptor states are charged if the Fermi energy is below/above the charge transition level, respectively

Intrinsic and extrinsic defects can both be classified as donors, acceptors, or neutral species. Donors and acceptors act as *dopants* as they have a different valence than the nominal lattice site. Some species can also be ambipolar, i.e., they can be either a donor or an acceptor, depending on the Fermi energy of the material. Ambipolar defects are, e.g., hydrogen [24] or oxygen interstitials [25]. Many defects can change their valence in dependence on the Fermi energy. This is illustrated for an arbitrary donor and an arbitrary acceptor species with two different valence states in Fig. 3.

The two charge states of the donor and acceptor species can be described by the *charge transition levels* (CTLs) attributed to them. Considering the ionisation reactions of donors and acceptors,

$$D \rightarrow D^+ + e^- \tag{4a}$$

$$A \rightarrow A^- + h^+ \tag{4b}$$

occupied donor states and unoccupied acceptor states are electrically neutral. As the occupation of the states is given by the Fermi energy, donors are neutral for $E_F > E_D$

and acceptors for $E_F < E_A$, where E_D and E_A are the CTLs of the donors and the acceptors, respectively. The charge transition levels are not real energy levels, they rather correspond to the value of the electron chemical potential, for which the charged / uncharged defect state is energetically more favorable.

Valence changes of defects occur particularly for defects with charge transition levels deep inside the energy gap. This is often the case for transition metals, which can have multiple CTLs inside the band gap. The charge state of such species thus depends crucially on the position of the Fermi energy, which is determined by the overall charge neutrality and by the concentrations and transition levels of all charged defects. For Fe-doped $BaTiO_3$, for example, the valence of Fe can vary from 2+ for strongly reduced samples with a high concentration of oxygen vacancies and a Fermi energy near the conduction band minimum [26] up to 5+, if the Fermi energy is sufficiently lowered by substitution of Ba with Na [27]. For certain Fermi energies, a defect can be neutral and then does not need charge compensation. An example for such a defect is the oxygen vacancy in ZnO, which is a deep double donor with a CTL about 0.7 eV below the conduction band minimum [28]. Small amounts of Al impurities, which form donor states inside the conduction band in ZnO, will then fix the Fermi energy close to the conduction band and thus render all oxygen vacancies neutral. These neutral vacancies can then be present in high concentrations without requiring charge compensation allowing for huge understoichiometric oxygen content. The electrons trapped in the neutral vacancies can be released and affect electrical properties [29].

Based on simple electrostatic considerations, a rule of thumb for the occurrence of defects in materials with different ionicity can be derived. The electrostatic energy of a sphere with radius r with a charge q is given by:

$$E = \frac{q^2}{r} \tag{5}$$

With increasing ionicity, i.e., with the difference in the number of valence electrons between a cation A and an anion

Table 1 Nominal charge states of different defects in semiconducting compounds with different ionicity. Group IV elemental materials, e.g. Si, are purely covalent, III-V compounds, e.g. GaAs, II-VI compounds, e.g. ZnS, and I-VII compounds, e.g. KCl and AgCl, exhibit increasing ionicity
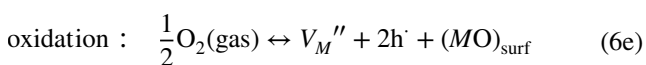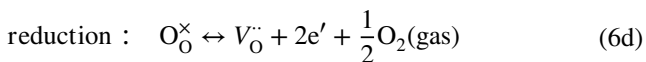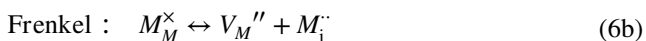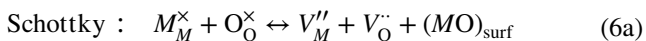
compound	IV	III-V	II-VI	I-VII
ionicity				
vacancies and interstitials				
charge	± 4	± 3	± 2	± 1
ΔH_D				
antisites				
charge	-	± 2	± 4	± 6
ΔH_D				

X of a compound *AX*, the formal charge of vacancies and interstitials decreases, while the charge of antisite defects decreases. The resulting trends are summarized in Table 1. Lowest formation enthalpies are expected for vacancies and interstitials in alkali-halides. Considerable vacancy and interstitial concentrations will still be present for the divalent ions, i.e., for oxides and chalcogenides, but their formation energies will increase with decreasing ionicity. The opposite trend is expected for antisite defects, which more frequently occur in III-V semiconducting compounds.

2.2.2 Defect thermodynamics

The thermodynamics of point defects can be approached in two ways. A detailed comparison of the two approaches would be too extensive for this contribution. Instead, only a brief introduction to the two approaches describing defect thermodynamics will be given here. For more details, the readers are referred to textbooks and review articles [13, 30].

The original and widely used approach to describe the thermodynamics of point defects in solids is *defect chemistry*, in which defect concentrations are obtained from defect reactions (see, e.g., [13]). These reactions involve different defect species in order to maintain charge neutrality. Example defect reactions are the Schottky and Frenkel defect pairs, and the electron-hole pair generation. For an oxide with a divalent cation, these are:

$$\text{Schottky}: \quad M_M^\times + O_O^\times \leftrightarrow V_M'' + V_O^{\cdot\cdot} + (MO)_{\text{surf}} \tag{6a}$$

$$\text{Frenkel}: \quad M_M^\times \leftrightarrow V_M'' + M_i^{\cdot\cdot} \tag{6b}$$

$$\text{electronic}: \quad nil \leftrightarrow e' + h^\cdot \tag{6c}$$

$$\text{reduction}: \quad O_O^\times \leftrightarrow V_O^{\cdot\cdot} + 2e' + \frac{1}{2}O_2(\text{gas}) \tag{6d}$$

$$\text{oxidation}: \quad \frac{1}{2}O_2(\text{gas}) \leftrightarrow V_M'' + 2h^\cdot + (MO)_{\text{surf}} \tag{6e}$$

where the *Kröger-Vink notation* has been used. The set of equations 6 includes the reduction reaction, which results in changes of stoichiometry and which connects the ionic and the electronic defect reactions. The Anti-Schottky and Anti-Frenkel defect reactions are not included but mentioned for completeness. Also not included in this brief treatment are the ionisation reactions of the ionic defect species. This corresponds to the assumption that they are always doubly charged. The defect reactions (6) are associated with *mass action laws*:

$$\text{S}: \quad K_S = \exp\left(-\frac{\Delta G_S}{k_B T}\right) = [V_M''] \cdot [V_O^{\cdot\cdot}] \tag{7a}$$

$$\text{F}: \quad K_F = \exp\left(-\frac{\Delta G_F}{k_B T}\right) = [V_M''] \cdot [M_i^{\cdot\cdot}] \tag{7b}$$

$$\text{el}: \quad K_{el} = \exp\left(-\frac{E_g}{k_B T}\right) = [e'] \cdot [h^\cdot] \tag{7c}$$

$$\text{red}: \quad K_{red} = \exp\left(-\frac{\Delta G_{red}}{k_B T}\right) = [V_O^{\cdot\cdot}] \cdot [e']^2 \cdot pO_2^{1/2} \tag{7d}$$

$$\text{ox}: \quad K_{ox} = \exp\left(-\frac{\Delta G_{ox}}{k_B T}\right) = [V_M''] \cdot [h^\cdot]^2 \cdot pO_2^{-1/2} \tag{7e}$$

where *K* and ΔG are the equilibrium constant and free formation enthalpy of the respective defect reaction, E_g is the energy gap, [...] are the mole fractions of the defects, and pO_2 is the oxygen partial pressure.

The set of equations 7 can be solved by employing the *charge neutrality* condition. Assuming Schottky disorder to dominate the ionic defect reactions, i.e. only metal and oxygen vacancies are considered as ionic defect species, the charge neutrality is:

$$2 \cdot N(V_O^{\cdot\cdot}) + p = 2 \cdot N(V_M'') + n \tag{8}$$

Note that defect concentrations are used in Eq. 8, while the mass action laws (7) contain mole fractions ([..]). Defect concentrations and mole fractions are connected via the concentration of defect sites, which are the concentration of atoms for ionic defects and the effective density of states for the electronic defects (for the latter see Section 3.1). Having solved the set of mass action laws and the charge neutrality condition, the defect concentrations can be plotted versus the oxygen partial pressure, pO_2. Schematic diagrams employ the *Brouwer approximation*, which assumes that the charge neutrality conditions for low, medium, and high oxygen partial pressure can be approximated by:

$$\text{low}: \quad 2 \cdot N(V_O^{\cdot\cdot}) \approx n \tag{9a}$$

$$\text{mid}: \quad \begin{cases} N(V_O^{\cdot\cdot}) & \approx N(V_M'') \\ n & \approx p \end{cases} \tag{9b}$$

$$\text{high}: \quad p \approx 2 \cdot N(V_M'') \tag{9c}$$

For intermediate oxygen partial pressures, either the Schottky or the electronic defect equilibrium are dominating depending on the relative magnitude of ΔG_S and E_g. An example for a Brouwer diagram is displayed in Fig. 4.

The logarithmic defect concentrations exhibit the well-known power law dependencies on oxygen partial pressure with the exponents given in Fig. 4
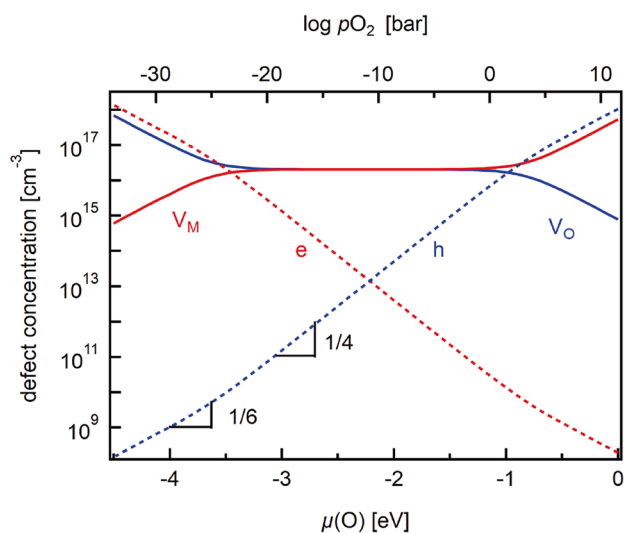
Fig. 4 Defect concentrations of a hypothetical compound with composition MO with $N_M = N_O = 3 \cdot 10^{22}$ cm^{-3}, efective masses of electrons and holes equal to the free electron mass, and dominating Schottky disorder at $T = 1000$ K. The parameters used for the calculation are $\Delta G_S = 2.45$ eV, $\Delta G_{red} = 5.5$ eV, and $E_g = 3.0$ eV

Fig. 5 Defect formation energies in dependence on the electron chemical potential of a hypothetical compound MO with Schottky disorder. The formation energies are given at the left in the metal-rich limit ($\mu_O = -4.5$ eV) and at the right in the oxygen-rich limit ($\mu_O = 0$ eV). The difference in defect formation energies between the two graphs corresponds to the formation enthalpy of the compound μ_{MO}, which is arbitrarily set to -4.5 eV. The defect concentrations in dependence on μ_O and pO$_2$ obtained using the given dependence of defect formation enthalpies are identical to those displayed in Fig. 4

A different approach to determine defect concentrations is based on *ab-initio* calculations [30, 31]. The enthalpy for the formation of a lattice defect can thereby be obtained from total energy calculations using supercells according to:

$$\Delta H_D = H_{defect}^q - H_{ideal} + q \cdot (\mu_e - E_{VB}) + \Sigma_i (\Delta n_i \mu_i) \quad (10)$$

where H_{defect}^q and H_{ideal} are the enthalpies of the supercell with a defect of charge q and of the ideal supercell, respectively. Δn_i and μ_i are the number of species, i, that are removed from or added to the supercell in order to include the defect. As above, μ_e is the electron chemical potential. In contrast to the defect chemistry approach, every defect is treated individually rather than in pairs. In order to obtain the equilibrium defect concentrations for fixed chemical potentials, the concentrations have to be calculated as a function of the electron chemical potential. In a second step, the equilibrium Fermi energy is obtained by finding the unique value of the electron chemical potential, at which charge neutrality is achieved. In order to find the dependence on oxygen partial pressure, which is connected to the chemical potential of oxygen, the calculations have to be repeated for the range of chemical potentials at which the compound is stable.

An example for the dependence of defect formation enthalpies on the electron chemical potential under most oxidising and most reducing conditions is given in Fig. 5. The formation enthalpies of neutral metal and oxygen
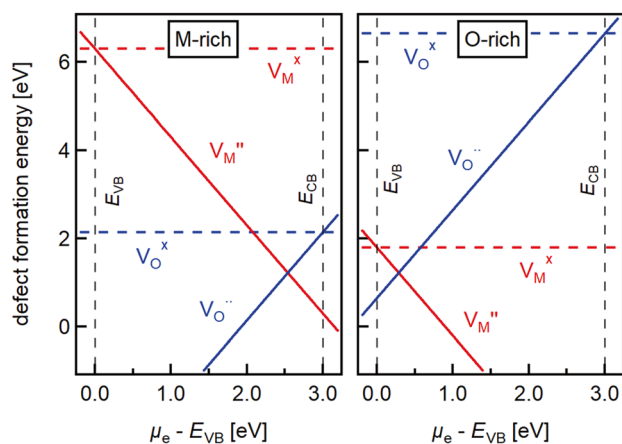
vacancies are included in Fig. 5. These are set in a way that the vacancies remain doubly charged for all values of the electron chemical potential inside the energy gap. The formation enthalpies of singly charged vacancies are set to values high enough to not show up in the graphs. The defect concentrations in dependence on oxygen partial pressure obtained using the defect formation enthalpies from Fig. 5 are identical to those displayed in Fig. 4. The connection is evident for the energy of the Schottky defect pair (2.45 eV in Fig. 4), which is simply the sum of the defect formation enthalpies of the charged metal and oxygen vacancies in Fig. 5. The sum of the two is also independent on the electron and the oxygen chemical potentials.

The defect chemistry and the physical approach of considering defect formation energies in dependence on the electron chemical potential and the chemical potentials of the constituents are fully equivalent and provide identical equilibrium defect concentrations. While the defect chemistry description of point defect thermodynamics is a powerful, intuitive, and very useful concept, the second (physical) approach is directly suitable for the discussion of Fermi level engineering in this contribution. The principle advantage of the physical approach is that all potentially contributing defects can be treated on the same basis, thereby providing unanimous explanations for the prevailing defect species and charge compensation mechanism.

3 The Fermi energy and charge compensation

3.1 Electronic charge compensation

Doping of classical semiconductors, such as Si, which can be very accurately controlled down to concentrations of parts per billion (ppb), results in the occupation of states in the conduction band (free electrons) or in the emptying of states in the valence band (free holes). The positive/negative charge of the donor/acceptor is then compensated by the negative/positive charge of the electron/hole. Independent on the material, its band gap, and any other defects present, the electron concentration, n, and hole concentration, p, can be obtained using the integral over the density of electronic states multiplied by the occupation of the states according to [12]:

$$n = \int_{E_{CB}}^{\infty} N_{CB}(E) \cdot f(E)\, dE \tag{11a}$$

$$p = \int_{-\infty}^{E_{VB}} N_{VB}(E) \cdot (1 - f(E))\, dE \tag{11b}$$

where E_{VB} and E_{CB} are the energy of the valence band maximum (VBM) and conduction band minimum (CBM), $N_{VB}(E)$ and $N_{CB}(E)$ are the density of states in the valence and the conduction band, and $f(E)$ is the Fermi distribution function. The integrals (11) can be solved analytically if two classical approximations are involved [12]: The parabolic band approximation assumes that the energy in the conduction and in the valence band depends parabolically on the electron's momentum ($E \propto k^2$). This assumption is valid as long as only electronic states very close to E_{CB} and E_{VB} are involved. The approximation results in a square-root dependence of the density of states ($N_{VB}(E) \propto \sqrt{E_{VB} - E}$ and $N_{CB}(E) \propto \sqrt{E - E_{CB}}$). The second approximation is that of non-degenerate semiconductors, which assume that the Fermi energy stays at least $3 k_B T$ away from the band edges ($E_F - E_{VB} > 3 k_B T$ and $E_{CB} - E_F > 3 k_B T$). The Fermi distribution function can then be replaced by a Boltzmann function. Eventually, the electron and hole concentrations become:

$$n = N_C \exp\left(-\frac{E_{CB} - E_F}{k_B T}\right) \tag{12a}$$

$$p = N_V \exp\left(-\frac{E_F - E_{VB}}{k_B T}\right) \tag{12b}$$

with

$$N_{C,V} = 2\left(\frac{2\pi m_{e,h}^* k_B T}{h^2}\right)^{3/2} \tag{12c}$$

where $N_{C,V}$ are the effective densities of states in the conduction and valence band, which depend on the effective masses, $m_{e,h}^*$, of the carriers (the inverse curvature of the energy bands [12, 21]). The concentration of free electrons and holes depends directly on the energetic distance of the Fermi energy and either the valence band maximum or the conduction band minimum. The product of n and p is independent of the Fermi energy and corresponds to the law of mass action for electron-hole generation in defect chemistry (Eq. 7c). The basis of semiconductor technology is the spatial control of charge carrier concentrations by doping. According to Eq. 12, this is equivalent to controlling the Fermi energy. Therefore, semiconductor technology, which enable a wide range of applications, including (light emitting) diodes, transistors, solar cells, sensors, varactors, microwave generators [12] can be considered as Fermi level engineering.

Electronic compensation, which leads to electronic conduction, in oxides is important for several applications, such as ceramic heating elements, membranes, and electrode materials for fuel cells and batteries. As an example, donor- (e.g. La or Nb) doped $BaTiO_3$ is an electron conductor, which is the basis for the PTCR effect [16, 32, 33] utilized in sensors and ceramic heating elements. The n-type conductivity in this compound disappears for donor concentrations > 0.1 %, which has been related to the segregation of cation vacancies to grain boundaries [34]. Evidently, donor doping does not only introduce electrons but also cation vacancies (partial ionic compensation), which is also reported for donor-doped $SrTiO_3$ [35]. In order to avoid electronic conductivity in $BaTiO_3$, which is crucial for the wide use of $BaTiO_3$ as dielectric in multilayer ceramic capacitors, it is doped with acceptors, such as Mg, Mn, or Fe [4]. In contrast to donor doping, acceptor doping of $BaTiO_3$ does not result in electronic but in ionic compensation, i.e. in the generation of oxygen vacancies.

The concentrations of electrons and holes in semiconductors, particularly in semiconductors with wide band gaps, are limited [36–38]. These limits are known as doping limits and correspond directly to a limitation of the Fermi energy. The mostly discussed origin of the limitation of the Fermi energy and carrier concentrations is *ionic compensation*, also known in semiconductor physics as *self-compensation*, which will be discussed in the following section. The key to achieve p-type doping in GaN, which enables blue light emitting diodes, is to kinetically suppress ionic compensation upon acceptor doping. This can be achieved by the addition of hydrogen, which is compensating acceptor doping during material synthesis and which can be removed afterwards at lower temperatures in order to activate the acceptors [39].

3.2 Ionic charge compensation

In general, ionic compensation is achieved by the formation of lattice defects, such as vacancies or interstitials, in response to the insertion of a charged defect. Oxygen ion conductors are mostly utilizing ionic compensation. The formation of oxygen vacancies in Y-stabilized ZrO_2 (YSZ) is, for example, induced by acceptor doping. Due to its effect on the polarization and strain hysteresis, acceptor and donor doping of piezoelectric materials are referred to as hard and soft doping, respectively [14]. The effects of doping in dielectrics and piezoelectrics are also discussed in terms of the ionic compensation mechanism [14, 40, 41]. However, not every acceptor or donor species generates the same properties. For example, resistance degradation is significantly different for Mn- and Mg-doped $BaTiO_3$ [42]. Such differences, which are important for application, can hardly be described by ionic compensation alone.

Here, the introduction of charged defects does not lead to electronic compensation but to the formation of ionic defects. Self- or ionic compensation is directly related to the dependence of the defect formation enthalpy of a defect, ΔH_D, on the Fermi energy and the chemical potential. The situation for a binary oxide MO with a divalent intrinsic donor and a divalent intrinsic acceptor defect, which is analogous to that displayed in Fig. 5, is illustrated in Fig. 6. For donor defects, such as oxygen vacancies, the formation enthalpy decreases with decreasing μ_e due to the energy, Ξ, gained by removing the electron from the defect (Fig. 6(a)). The resulting defect formation

enthalpies are plotted in dependence on μ_e in Fig. 6(b). For more oxidizing conditions, the formation enthalpy of the intrinsic donor is increased and that of the intrinsic acceptor decreased.

When decreasing the Fermi energy (e.g., by acceptor doping), the defect formation enthalpy of the intrinsic donor decreases until it approaches zero. A zero defect formation enthalpy would mean that the defect concentration is as high as the concentration of lattice sites. A condition that is obviously not compatible with the thermodynamic stability of the material. Therefore, the material is only stable if the defect (free) formation enthalpies are positive. This requires that the Fermi energy remains within the range indicated as $\Delta\mu_e$(red) or $\Delta\mu_e$(ox) in Fig. 6(b). The accessible range of the Fermi energy varies with the chemical boundary conditions due to the dependence of the defect formation enthalpies on the chemical potentials of the constituents (Eq. 10). A high activity of a species would, for example, lower the formation enthalpy of a vacancy of that species.

Although the calculation of defect formation enthalpies using density functional theory has become routine [30], there is still a lack of quantitative agreement between theory and experiment regarding both formation enthalpies and charge transition levels (CTLs) of the defects (E_D and E_A in Fig. 6). This discrepancy is even observed with the most accurate calculations using hybrid functionals, which reproduce experimental band gaps quite well. It has been predicted, for example, that the maximum electron concentration in donor-doped SnO_2 is higher than that in donor-doped In_2O_3 [43], which contrasts with experiment [44]. The recently determined $Fe^{2+/3+}$
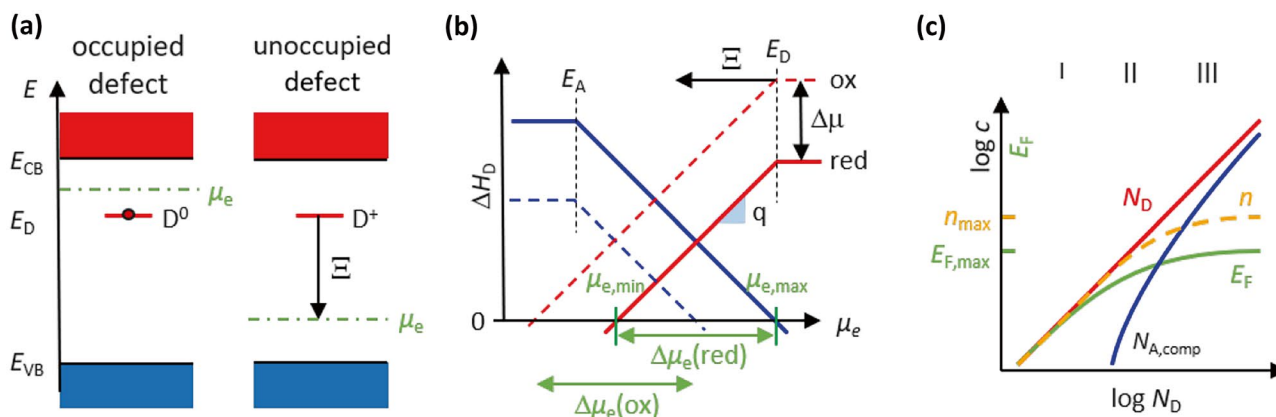

Fig. 6 Dependence of defect formation enthalpies on the Fermi energy as origin for ionic (self) compensation and doping limits: **(a)** The removal of electron(s) from a donor results in an energy gain Ξ, if the Fermi energy is below the charge transition level of the donor E_D; **(b)** defect formation enthalpies of intrinsic acceptor (blue) and donor (red) defects according to Eq. 10 for most oxidizing (ox) and reducing (red) conditions, differing by $\Delta\mu$, which corresponds to the formation enthalpy of the compound. Doping with acceptors (donors) lowers (raises) the Fermi energy, which reduces the formation enthalpies of compensating intrinsic donor (acceptor) defects. The limits

of the Fermi energy are reached once the defect formation enthalpies approach 0, resulting in spontaneous formation of defects. The limits of μ_e are indicated for reducing conditions; **(c)** concentrations of electrons, n, and intrinsic acceptor defects, $N_{A,comp}$, and equilibrium Fermi energy in dependence on donor concentration. At low donor concentration (region I), the donors are compensated by electrons, while at high donor concentration (region III) the electron concentration and the Fermi energy saturate and the donors become mostly compensated by intrinsic acceptor defects
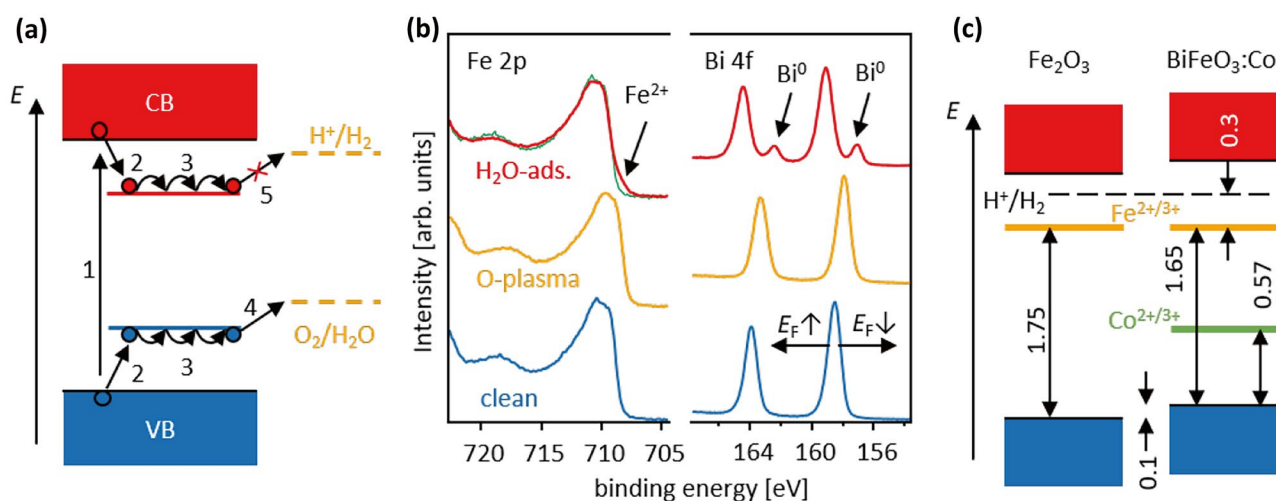
Fig. 7 (**a**) Schematic illustration of the influence of self-trapping on photocatalytic water splitting. Electrons and holes generated by optical absorption (1) will be self-trapped (2) and transported to the surface by a (slow) hopping process (3). In the example, oxidation of water by self-trapped holes (4) is energetically favorable, in contrast to the reduction of water by self-trapped electrons (5), which requires an additional activation energy; (**b**) Fe2p and Bi4f X-ray photoelectron spectra of a $BiFeO_3$ thin film after surface cleaning, oxygen plasma treatment and after room temperature water exposure [54]. The different treatments induce pronounced changes of the Fermi energy as indicated by the parallel binding energy shifts of Fe and Bi. The adsorption of water results in a considerable upward shift of the Fermi energy and a concomitant reduction of Fe and Bi; (**c**) energy band diagram of Fe_2O_3 and $BiFeO_3$ showing the alignment of the $Fe^{2+/3+}$ charge transition level in both materials and the $Co^{2+/3+}$ transition level in Co-doped $BiFeO_3$

charge transition levels in $SrTiO_3$ and $BaTiO_3$ [26] also do not agree with recent calculations [45].

3.3 Self-trapping of electrons and holes

Self-trapping of holes or electrons is also known as polaron formation [46]. The energy levels of the trapped charges correspond to electrochemical oxidation and reduction potentials [47, 48], which indicate at which Fermi energy a cation or anion is oxidized or reduced. As an example, Fe^{3+} in Fe_2O_3 and $LaFeO_3$ can be oxidized to Fe^{4+} or reduced to Fe^{2+} [17, 49]. As the material is only thermodynamically stable for the proper oxidation states of the species, the oxidation and reduction potentials constitute a lower and an upper limit for the Fermi energy. In contrast to the Fermi energy confinement induced by ionic compensation, the confinement induced by valence changes is not limited to high temperatures as no diffusion of ions is required for self-trapping of electrons and holes. It also does not depend on the chemical boundary conditions (oxygen activity).

The valence change of host ions constitutes an important compensation mechanism for charged defects. Electrons typically trap on cationic sites as the anion orbitals do not contribute substantially to the conduction band states. In contrast, holes can be trapped on cations and on anions [50]. Self-trapping on cation sites is most prominent for 3d transition metals [17]. However, valence changes are also observed on 4d- and 5d-transition metals (e.g., Mo,

W, Nb [50]) although these states are less localized due to the larger extension of their d-orbitals. Hole trapping has further been reported to occur on Pb ions in $Pb(Zr,Ti)O_3$ [51]. Eventually, electrons and holes introduced by optical absorption, charge injection, doping, or polarization, will be trapped (localized) at a lattice site in many materials, particularly in oxides.

The self-trapping of photo-excited electrons and holes is illustrated in Fig. 7(a). Subsequent transport of the trapped charges to a surface for charge transfer will then occur via a hopping process. For electrons (holes), the charge transfer is more efficient when the electron (hole) polaron energy level, e_p (h_p), is higher (lower) than the receiving energy level. The example in Fig. 7(a) schematically illustrates the redox levels involved in water splitting. Here, hydrogen evolution would be less efficient than oxygen evolution. Such an electron self-trapping can, for example, explain the low photocatalytic water splitting efficiency of Fe_2O_3, which should otherwise have an ideal band gap of 2.2 eV for this application [52]. In the case of hematite Fe_2O_3, the observed trapping level at 0.5 eV below the conduction band minimum corresponds very well with defect calculations [53].

Reduction and oxidation potentials of a series of compounds, such as Fe_2O_3 [52], $BiFeO_3$ [54], $BiVO_4$ [55], and other compounds have been identified by photoelectron spectroscopy. The phenomenon is illustrated for $BiFeO_3$ in Fig. 7(b), which shows Fe2p and Bi4f XPS core level spectra after surface cleaning, a subsequent oxidation treatment, and a final reduction treatment [54]. Oxidation and reduction

lower and raise the Fermi energy, respectively, which is evident from the shifts of the binding energies. The reduction of Fe and Bi is directly observed in the spectra. Comparable to $BiFeO_3$, simultaneous reduction of Bi and V is observed for $BiVO_4$ [55], an important oxide absorber material for photoelectrochemical water splitting. While the limitation of the Fermi energy can be detrimental for charge transfer in photo- or electrochemical processes, it is expected to be beneficial for dielectrics and piezoelectrics as it guarantees a high electrical resistivity by confining the Fermi energy away from the band edges [54].

3.4 The solubility of dopants

In general, heterovalent substituents may have a rather low solubility, resulting in segregation of dopants to surfaces or grain boundaries or the formation of secondary phases, sometimes already for doping concentrations below 1 % (see, for example, [14, 56]). Segregation of dopants can be intentionally used, as it affects the microstructure evolution either by formation of liquid phases [57] or by suppression of grain boundary movement via the solute drag effect [58]. Grain boundary segregation is also fundamental to establish the potential barriers at grain boundaries, being particularly relevant as the origin of the highly nonlinear current-voltage characteristics of ZnO varistors [59]. Potential barriers at surfaces can substantially decrease ionic conductivity and surface ion exchange [60]. Another related effect of segregation is the controlled precipitation of metallic nanoparticles at oxide surfaces at high temperature, called exsolution [61], which can be beneficial for (electro-)catalytic applications. Conversely, segregation of Sr acceptor dopants to the surface of mixed ionic-electronic fuel cell cathode materials, such as (La,Sr)$CoO_{3-\delta}$ and $Sr(Ti,Fe)O_3$, is detrimental to the surface oxygen exchange behavior [62–65].

Segregation occurs as the formation enthalpy of defects in the bulk is different from that at surfaces or grain boundaries [66, 67]. Segregation can originate from elastic forces, which are high for highly size mismatched ions [68, 69]. However, there is also experimental evidence that segregation is coupled to the Fermi energy. The concentration of Sn at surfaces of Sn-doped In_2O_3 (ITO) thin films is depicted in Fig. 8 as a function of the electron concentration of the films [70]. It is evident that the surface concentration of the donor dopant increases for carrier concentrations $> 10^{20}$ cm^{-3}. It can be excluded that this is an artefact of sample preparation, as near ambient pressure XPS reveals that the surface Sn concentration changes reversibly upon oxidation and reduction [71]. The segregation is related to the defect formation enthalpy of the Sn_{In} donor defect, which increases with increasing Fermi energy [72], for the same reason as for self-compensating intrinsic defects (see Fig. 6(b)). As long as the formation enthalpy of Sn_{In} is negative, all donors can be
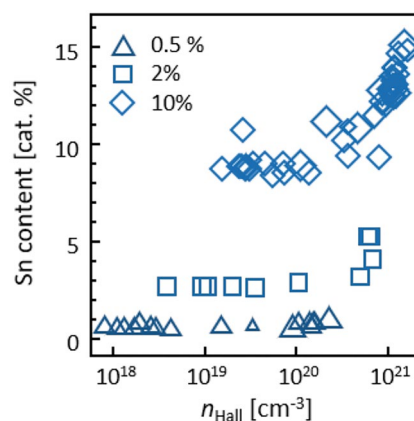

Fig. 8 Sn surface concentrations of 0.5, 2, and 10 % Sn-doped In_2O_3 from in situ XPS as a function of carrier concentrations n_H from Hall effect measurements [70]

incorporated. With increasing doping, the Fermi energy rises and the formation enthalpy of the Sn_{In} donor will become positive. The dopant site fraction determining the solubility is then given by $\exp(-\Delta H_D/k_B T)$. Any donors supplied in excess to this concentration cannot be dissolved and the donor will segregate if sufficiently mobile. The dependency of the defect formation enthalpy of the donors explains that the "doping efficiency" decreases with increasing doping concentration, which has been described in transparent conductive oxides (see, e.g., [73]).

3.5 The Fermi energy as universal descriptor for comparing compensation mechanisms

The description above illustrates that all possible ways of a material to react on doping can be described by their dependence on the Fermi energy. While isovalent substitution of a lattice species results in a change of the density of states, heterovalent substitution is always accompanied by a shift of the Fermi energy. Donor doping, which is characterized by the donation of an electron to the lattice and a positive charge residing on the donor site, results in an upward shift of the Fermi energy. On the other hand, acceptor doping results in a downward shift of the Fermi energy. The shift of the Fermi energy is changing the formation enthalpies of all defects, which could be involved in the compensation of the charge of the dopant. Raising the Fermi energy decreases the formation enthalpy i) of free electrons in the conduction band, ii) of intrinsic acceptor defects, such as metal vacancies or anion interstitials, and iii) for the trapping of electrons on cation sites. In addition, raising the Fermi energy iv) increases the probability for a neutralization of the dopant, which will eliminate the requirement for further charge compensation and v) increases the formation enthalpy of the donor and thereby reduces its solubility,

Table 2 Possible ways of how a material can react on heterovalent substitution (doping)

doping	compensation
donor	electron in CB
$D \rightarrow D^+ + e^-$	trapped electron
raises E_F	intrinsic acceptor (e.g. cation vacancy)
reducing	neutralization of donor
	donor segregation
acceptor	hole in VB
$A \rightarrow A^- + h^+$	trapped hole
lowers E_F	intrinsic donor (e.g. anion vacancy)
oxidizing	neutralization of acceptor
	acceptor segregation

eventually resulting in a segregation of the dopant. Lowering the Fermi energy by acceptor doping has analogous effects for free and trapped holes, intrinsic donors, acceptor neutralization, and acceptor segregation. The different ways to react on doping are summarized in Table 2.

The different mechanisms for compensation of charged defects can be summarized in the charge neutrality conditions. Instead of using a single charge neutrality equation, two independent equations are used for donor and acceptor doping in order to emphasize the effect of increasing and lowering the Fermi energy, respectively. We further simplify the equations by assuming that all defects are either neutral or singly charged and by taking the square brackets, [..], to denominate concentrations. In the two charge neutrality equations (13), the (intrinsic) lattice defects, A_{lat} and D_{lat}, are those introduced by the ionic compensation mechanism. Self-trapping of electrons on cations and of holes on cations and anions are the last terms in the equations. In extension to the simplified version given in Section 2.2 (Eq. 8), the charge neutrality equations for donor (D) and acceptor (A) doping can then be written as:

$$[D^+] = [D] - [D^0] - [D^{seg}]$$
$$= [e^-] + [A_{lat}^-] + [Cat_{Cat}^-] \tag{13a}$$

$$[A^-] = [A] - [A^0] - [A^{seg}]$$
$$= [h^+] + [D_{lat}^+] + [Cat_{Cat}^+] + [An_{An}^+] \tag{13b}$$

The different compensation mechanisms, neutralization and segregation of dopants, electronic and ionic compensation, and self-trapping on host ions, do all depend on the Fermi energy and can therefore be compared using a common energy axis as illustrated in Fig. 9. First of all, the concentration of electrons and holes given in Eq. 12 can formally be described with Eq. 3 by using defect formation enthalpies becoming zero at the band edges as depicted in Fig. 9(b). The defect formation enthalpies of intrinsic donors and acceptors as a function of the Fermi energy (same as in Fig. 6) and the

formation enthalpies of self-trapped electrons and holes are depicted in Fig. 9(c) and (d), respectively. Self-trapping occurs for Fermi energies where the defect formation enthalpies are negative. In both cases, the material is only stable for Fermi energies at which the defect formation enthalpies are positive.

The formation enthalpy of a donor with a charge transition level E_D is provided in Fig. 9(e). For $E_F > E_D$, the donor becomes neutral and requires no charge compensation. If the donor is the only ionic defect, the Fermi energy will be constrained to $E_F < E_D$. The formation enthalpy of an extrinsic donor species and its effect on the maximum solubility $[D]_{max}$ of the donor is shown in Fig. 9(f). For Fermi energies where the formation enthalpy ΔH_D is negative, there is no constraint and all supplied donors can be incorporated as donors in the lattice. For higher Fermi energies, the donor formation enthalpy may become positive. In this case, the maximum concentration of donors becomes $\exp(\Delta H_D)$ times the concentration of lattice sites, which means that it decreases exponentially with increasing Fermi energy as indicated by the red curve in Fig. 9(f).

4 Fermi level engineering

In order to control material properties, it is necessary to adjust the Fermi energy with respect to the band edges and the charge transition levels and formation enthalpies of the involved defects. Eventually, these quantities are changing with composition and the selection of dopants. To this end, Fermi level engineering is not new as changing the composition and doping is the general strategy for adjusting material design. However, the role of composition and the choice of dopants are not completely understood and materials are often optimized empirically, sometimes benefiting from serendipity. With the concept outlined in Section 3.5, the role of composition and dopant species and concentrations can be rationalized and ideally be used in order to predict resulting material properties.

With the example of two hypothetical materials, Fig. 10 illustrates the effect of the different quantities. The different composition results in a different density of states and different energies of the valence band maximum and conduction band minimum. Moving E_{VB} and E_{CB} up or down will affect the possibility for electronic compensation. Moving the different defect energy levels up or down will change the accessible range of the Fermi energy. The energy levels of dopants are affected by the dopant species, but also by the composition of the host material. The energy levels of ionic defects (in Fig. 10 vacancies are exemplarily used) and of the valence changes, are also affected by the composition. For the examples given in Fig. 10, cation and anion vacancies are the limiting factor in material X, resulting in ionic compensation of both donor and acceptor doping. In material Y, the chosen donor determines the upper limit of the Fermi energy while oxidation of a cation
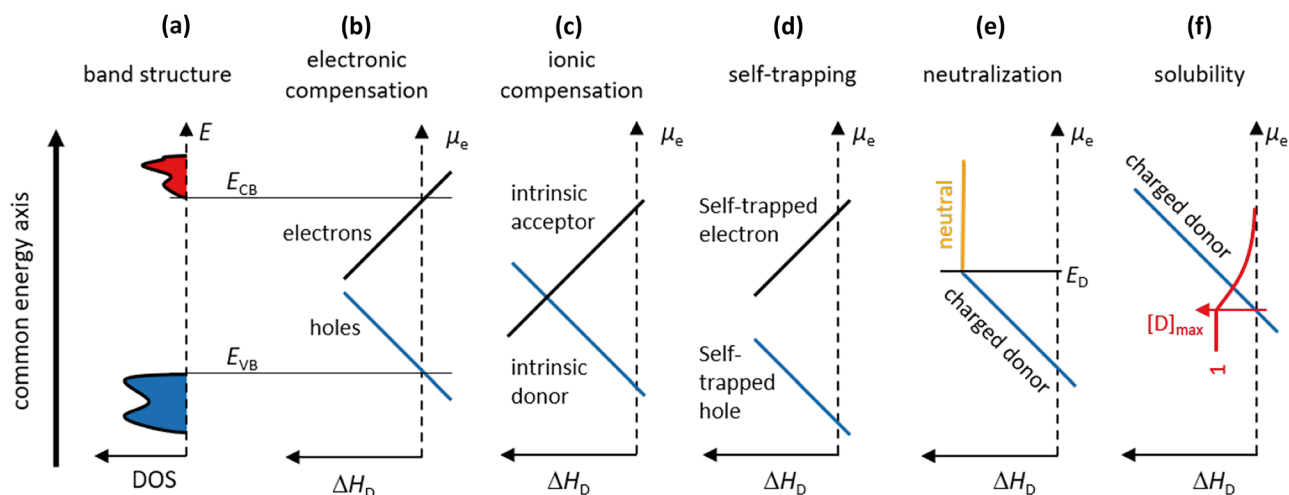
Fig. 9 (**a**) Density of states of a compound with valence band maximum at E_{VB} and a conduction band minimum at E_{CB}; (**b**) - (**f**) defect formation enthalpies of different defects in dependence on μ_e; (**b**) formal formation enthalpies of electrons and holes in Boltzmann's approximation, Eq. 12; (**c**) formation enthalpies ΔH_D of an intrinsic donor and an intrinsic acceptor defect. The material is only stable for values of μ_e where the defect formation enthalpies are positive; (**d**) formation enthalpies of self-trapped electrons and holes. Self-trapping occurs when the defect formation enthalpies are negative. The material is only stable if the atoms have their nominal valence, that is when no self-trapping occurs; (**e**) formation enthalpy of a donor impurity with a charge transition energy E_D in dependence on μ_e. The donor becomes neutral for $\mu_e > E_D$; (**f**) formation enthalpy of a charged donor and the resulting maximum site fraction $[D]_{max}$, which can be occupied by the donor. As long as the formation enthalpy is negative, all supplied donor species can be incorporated, hence $[D]_{max}$. For positive formation enthalpies, the maximum number of incorporated donors cannot be higher than $\exp(-\Delta H_D / k_B T)$ times the concentration of lattice sites. The energy axis is common to all graphs

or anion determines the lower one. The different influences and potential strategies for Fermi level engineering are outlined in the following sections.

4.1 Positions of the energy bands

The possibility for electronic compensation is directly related to the energetic positions of the valence band maximum and
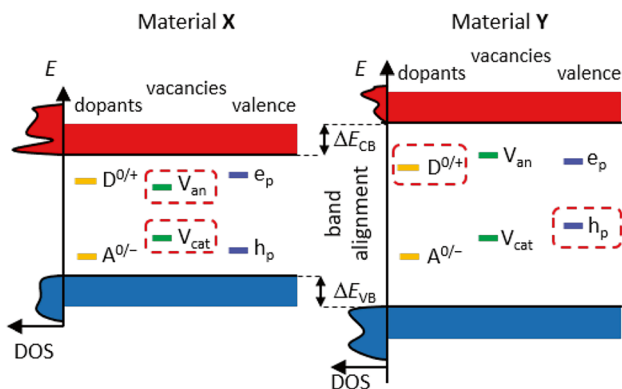

Fig. 10 Two hypothetical materials containing different dopants, energy levels of cation and anion vacancies, and electron and hole polaron levels related to the valence changes of cations and/or anions. The different positions of the valence band maximum and conduction band minimum are related to the different density of states. The different defect energy levels are also related to the different material composition. Defects limiting the Fermi energy are emphasized by the dashed red boxes

the conduction band minimum, E_{VB} and E_{CB}, which determine the fundamental energy gap $E_g = E_{CB} - E_{VB}$. The energy gap is often, but not always [74–76], directly related to optical absorption. Many photocatalytic materials, such as TiO$_2$ [77], have rather high band gaps and can therefore utilize only a small fraction of the sunlight spectrum. This shortcoming has led to considerable efforts to lower their band gaps. One strategy is the substitution of oxygen by nitrogen [78, 79]. As the N2p level is considerably higher in energy than the O2p level [80], (oxy-)nitrides do generally have higher E_{VB} and thus lower band gaps than the respective oxides [81]. The energy band alignment is further important for the alignment of defect energy levels, which has been discussed for transition metal dopants [82, 83], hydrogen impurities [24], and oxygen vacancies [84] (see also Section 4.4).

The energy band alignment of different oxides, determined by X-ray photoelectron spectroscopy (XPS) of intimate contacts between materials, is provided in Fig. 11 [85, 86]. The bands are aligned relative to the energy bands of any reference material, for example SnO$_2$ as in Fig. 11. The positions of the VBMs can be rationalized by considering the orbital contributions to the valence band density of states. The VBMs of SnO$_2$, ZnO, In$_2$O$_3$, anatase TiO$_2$, SrTiO$_3$, BaTiO$_3$, and LaAlO$_3$, where valence bands are formed by O2p states, have very similar E_{VB}. This observation is in line with the common anion rule [87], which has been originally proposed for III-V semiconductors but was
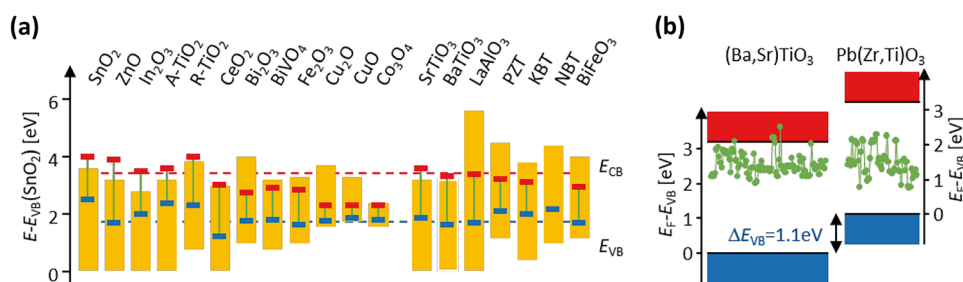
Fig. 11 (**a**) Energy band positions of different oxides as determined by interface experiments using X-ray photoelectron spectroscopy (XPS) [85, 86]. Yellow bars indicate the gap region. Blue and red horizontal bars indicate the lowest and highest Fermi energies measured using XPS for various sample preparations and treatments and at different interfaces. The dashed blue and red lines indicate the approximate lower and upper limits of the Fermi energy, respectively. Their position with respect to the band edges indicates for which materials electronic compensation can be expected; (**b**) Fermi energy positions measured using XPS for a series of $(Ba,Sr)TiO_3$ and $Pb(Zr,Ti)O_3$ thin films with aligned energy bands [93]. Each data point corresponds to a different sample

later discarded for these materials due to the effect of Fermi level pinning by induced gap states [88, 89]. Fermi level pinning by induced gap states is particularly pronounced for covalently bonded semiconductors. However, studies of the band alignment of oxides have revealed that Fermi level pinning is not important for oxides [85], which is connected to the ionic bonding character [90]. Nevertheless, considerable effort is required when measuring band alignment of ionic semiconductors using XPS, as Fermi level confinement by bulk defects (see Section 4.3 and [85]) has to be excluded by an adequate sample preparation. For example, the band alignment at the interface between Cu_2O and ZnO has been observed to vary by more than 1 eV depending on interface preparation [91]. Even though the common anion rule provides a rough explanation for the similar E_{VB} of many oxides, this information has to be treated with caution. An example is TiO_2, where the E_{VB} of the anatase modification is 0.7 eV lower than that of the rutile modification. This offset can be understood by the different overlap between the non-bonding $O2p_z$ orbitals in anatase and rutile [92].

The contribution of occupied d-orbitals to the valence band states, which hybridize with $O2p$ states, raises E_{VB} considerably. Examples in Fig. 11 are the Cu-containing oxides, Fe_2O_3, and Co_3O_4. In addition to nitrides and oxynitrides as well as Cu-based oxides and oxides with partially filled d-shells, higher VBM are also obtained in oxides containing cations with a high-lying filled s-shell. The latter include oxides with Pb^{2+}, Sn^{2+}, and Bi^{3+} ions, such as the ferroelectric $Pb(Zr,Ti)O_3$ (PZT) [93], $(Na_{1/2}Bi_{1/2})TiO_3$ (NBT), $BiFeO_3$ (BFO) [54, 94], photocatalytic $BiVO_4$ [95], the p-type thin film transistor material SnO [96], and the p-type conductor Ba_2BiTaO_6 [97].

In XPS studies, upper and lower limits of the Fermi level are observed when materials are treated in highly oxidizing and reducing conditions (see, e.g., [52, 54, 85]). These upper and lower limits, which are indicated in Fig. 11 for every material by the red and blue horizontal bars, can be assigned to the doping limits mentioned in Section 3.1. For many materials, these limits are at similar energy when the energy bands of the materials are arranged according to their determined energy band alignment. The agreement of the Fermi energy limits is further emphasized for $(Ba,Sr)TiO_3$ and $Pb(Zr,Ti)O_3$ in Fig. 11(b) [93]. Such a fundamental limitation of the Fermi energy has also been discussed for classical semiconductors [36, 37, 98]. A major consequence of these doping limits, which are ascribed to ionic compensation (see Section 3.1), is that room temperature n-type conducting materials require a low conduction band minimum and p-type materials a high valence band maximum. It is particularly difficult to lower the Fermi energy close to the VBM in oxides, in which the valence bands are formed only by $O2p$ states as in SnO_2, ZnO, $SrTiO_3$ or $BaTiO_3$. On the other hand, p-type conduction is clearly favored for oxides containing Cu due to their high E_{VB} [99–103].

Energy band positions of materials can be determined by different means [104]. In particular, the experimental approach using photoelectron spectroscopy has been intensively used since the 1980's [105, 106]. With this technique, an alignment with respect to the vacuum energy can be obtained by comparing the work functions of samples [107]. This approach is difficult as the work function, defined by the difference between the Fermi energy and the vacuum energy, varies with the Fermi energy and with surface dipoles. Even for clean, adsorbate-free surfaces, the work function of semiconducting oxides can vary by 2 eV, depending on oxygen activity and surface orientation, due to the influence of polarity [108–110]. In electrochemistry, band edge energies are commonly correlated with activity by comparison to redox potentials [111]. The alignments are extracted from electrochemical impedance studies of solid/electrolyte interfaces, where the flat band potential is determined from Mott-Schottky plots [112]. In these experiments, the typically used reference potential is the redox potential of the standard hydrogen electrode at pH = 0, which

Fig. 12 Schematic illustration of the electronic structure of different oxides. The central part reveals the schematic density of states for the valence and conduction bands with the orbital contributions. The top and bottom rows highlight the energy band dispersion of the highest occupied and the lowest unoccupied states. The O2*p* bands may also vary in energy depending on the Madelung potential of the oxide
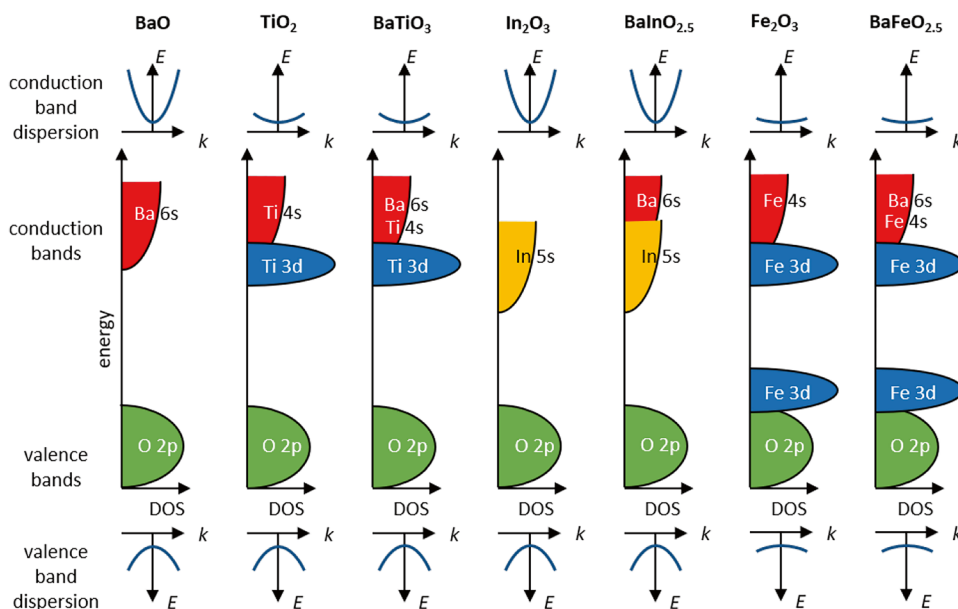
corresponds to an energy of $\approx 4.5\,$eV below the vacuum energy [113]. The alignment obtained from electrochemical measurements differ from that obtained using XPS at interfaces. One example for such a deviation is the energy band alignment of anatase and rutile TiO_2, where electrochemical measurements placed the E_{VB} of rutile $\approx 0.2\,$eV below that of anatase, while more recent DFT calculations and XPS measurements agree that the E_{VB} of rutile are $\approx 0.6\,$eV higher than that of anatase as indicated in Fig. 11 [92, 114, 115].

4.2 Orbital contributions to band structure and charge trapping

Simplified sketches of the electronic structure of a few oxide materials are given in Fig. 12. The materials described are all insulators, where the Fermi energy is located in the band gap between the filled valence band and the empty conduction band. The two parent compounds of the prototype perovskite $BaTiO_3$, BaO and TiO_2, are depicted on the left. BaO is an ionic compound in which the two 6*s* electrons of Ba are transferred to oxygen. Consequently, the filled valence band states are formed by the three O2*p* orbitals and the empty conduction band states by the Ba6*s* orbitals. The band gap of BaO is 4.8 eV. The valence band in TiO_2 is also mostly by O2*p* orbitals but the empty conduction band states are predominantly derived from Ti3*d*, which are lower in energy than the 4*s* orbitals. The band gap of TiO_2 is therefore only 3.2 eV. $BaTiO_3$ can, in principle, be considered as a superposition of the BaO and the TiO_2 states with an O2*p* valence band and a Ti3*d* conduction band. While the densities of states in the valence and conduction band in TiO_2 and $BaTiO_3$ are not identical due to the different symmetry and the

contribution of the Ba atoms, the band gap of $BaTiO_3$ is of the same magnitude as that of TiO_2.

The electronic configuration of In in $BaInO_{2.5}$ is $[Kr]4d^{10}$, with two electrons from the 5*s* and one from the 5*p* states transferred to oxygen. The In4*d* electrons are about 15 eV below the highest occupied states and do not contribute significantly to chemical bonding. The valence band is also formed by O2*p*, while the conduction band is mostly derived from In5*s* orbitals. The spatial extension of the 5*s* orbitals is larger than that of the 3*d* orbitals, resulting in a considerably stronger overlap and hence, to a broader energy band and a stronger dispersion $E(k)$, as indicated at the top of the graph. The strong overlap of neighboring In5*s* orbitals results in an energy gap of 2.8 eV [75].

The electronic structure of transition metal oxides is considerably more complex when the *d*-orbitals are partially occupied. Electron correlation and crystal field splitting result in charge, orbital, and spin ordering, which depend on the occupancy of the levels and therefore on the oxidation state [18, 116]. The situation for Fe^{3+}, which has a $3d^5$ electronic configuration, is straightforward for an octahedral environment, where the exchange splitting is considerably larger than the crystal field splitting into t_{2g} and e_g bands. The fully occupied spin-up states are energetically separated from the spin-down states. As sketched in Fig. 12, the states at the top of the valence band and at the bottom of the conduction band may then have considerable 3*d* character, leading to more localized electronic states and a higher probability for self-trapping of electronic carriers. The sketched electronic structure of Fe_2O_3 and the tendency for the formation of self-trapping on 3*d* orbitals is also reflected in the defect chemical descriptions, in which the band gap is modelled in terms of the transition $2Fe_{Fe}^{x} \rightarrow Fe_{Fe}' + Fe_{Fe}^{\cdot}$ rather

than by the formation of electron-hole pairs [17, 49]. As neither La nor Ba are expected to significantly hybridize with the O2p and Fe3d states, it is also expected that the states near the top of the valence band in BaFeO$_{2.5}$ have considerable Fe3d character. However, DFT calculations place the occupied Fe3d states at the bottom of the valence band [117, 118]. In this case, a lowering of the Fermi energy should result in the de-population of O2p states, which are more delocalized than Fe3d states. This is important as the center of the Op-band and its relative position to the transition metal d-states have been suggested as descriptors for oxygen incorporation at fuel cell cathode surfaces and for electrocatalytic oxygen evolution reactions [119, 120].

4.3 Fermi level confinement by doping

A possible role of doping is the introduction of charge transition levels into the energy gap (see Section 2.2). The CTLs can lead to a confinement of the Fermi energy, as illustrated in Fig. 13.

In the given example, an acceptor with a CTL E_A and a donor with a CTL E_D ($E_D > E_A$) of equal concentration are present in the material. The acceptor is charged for $E_F > E_A$ and the donor is charged for $E_F < E_D$. If the Fermi energy is in between the CTLs of the donor and acceptor, both charges compensate each other. The Fermi energy can be easily moved within this region. If the Fermi energy would be pushed below E_A or above E_D, the material will become charged. For high enough defect concentrations a layer of high charge density will be introduced, forming a narrow dipole, which effectively confines the Fermi energy inside the material to the uncharged region. While the confinement can be in both directions as in Fig. 13, a single upper or lower confinement can also be induced by a single dopant. An example for such a defect is the oxygen vacancy
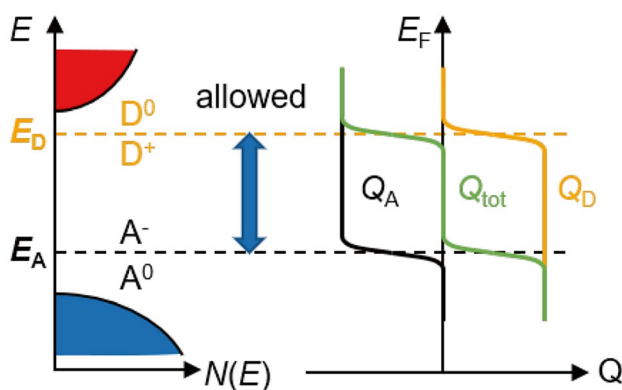

Fig. 13 Fermi level confinement by acceptors and donors of equal concentration. The positively charged donors and negatively charded acceptors compensate each other for $E_A < E_F < E_D$. For Fermi energies outside this range, the material becomes charged

in ZnO, which becomes neutral for Fermi energies closer than ≈ 0.7 eV below the Fermi energy [28, 121]. This charge transition level can result in a substantial effective variation of Schottky barrier heights and heterojunction energy band alignment [29, 91, 121, 122].

Another example for the confinement of the Fermi energy is given by water adsorption on BiFeO$_3$, which results in an upward shift of the Fermi energy and a reduction of Bi and Fe [54] (see also Fig. 7(b)). The reduction of Bi and Fe can be avoided by doping with cobalt. For low concentrations of oxygen vacancies, Co is present in BiFeO$_3$ as Co^{3+}. Adsorption of water then still raises the Fermi energy but only until the Co^{3+} is reduced to Co^{2+} at the respective CTL (Fig. 7(c)). This confinement of the Fermi energy by Co doping therefore prevents a further shift of the Fermi energy and the reduction of Bi and Fe.

The cobalt dopants in the latter example and the oxygen vacancies in ZnO offer a single charge transition level, which can limit either an upward or a downward shift of the Fermi energy. For an upward and a downward confinement of the Fermi energy, two CTLs are required as illustrated in Fig. 13. In principle, transition metal dopants offer such a possibility, as they exhibit multiple valence states. A more general strategy to confine the Fermi energy in both directions would be to use co-doping, which provides the flexibility for adjusting the upper and the lower limit of E_F separately by the charge transition levels of the donor and the acceptor. The co-doping approach will also be useful for a stronger confinement of the Fermi energy by increasing the density of the dopants. In the case of a single donor or acceptor, the solubility of the dopant is often limited (see also Section 3.4), but the addition of donors and acceptors in approximately equal amounts is charge neutral allowing for higher dopant concentrations. As example, Na and Bi doping of BaTiO$_3$ constitutes acceptor and donor species, respectively, and would substantially shift the Fermi energy. While doping of BaTiO$_3$ with larger amounts ($> 1\%$) of Na or Bi will likely result in formation of secondary phases, equivalent amounts of Na and Bi can incorporated up to a full substitution of Ba (solid solution (Na$_{1/2}$Bi$_{1/2}$)TiO$_3$-BaTiO$_3$ [123, 124]).

Confining the Fermi energy by addition of impurities with suitable valence levels might already be used in electroceramic materials as a consequence of empirical development of compositions. Eventually, the confinement of the Fermi energy can stabilize phases, electrical transport properties, and surface reactions against degradation.

4.4 The importance of defect energy levels

In principle, all compensation mechanisms are active in a material, but only one of them is prevailing and determining material properties in most cases. The prevailing
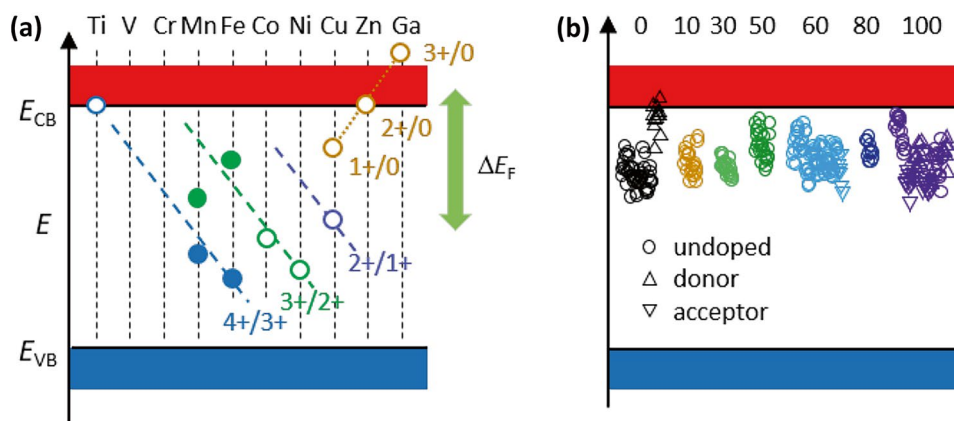
Fig. 14 (**a**) Energy levels of 3*d* transition metals in BaTiO₃. Filled symbols are from experimental determinations [26, 127] and open symbols are anticipated dependencies (see text). The green arrow at the right indicates the range of Fermi level positions in BaTiO₃ as derived from X-ray photoelectron spectroscopy [85, 131, 132]; (**b**) surface Fermi energies of several hundred (Ba,Sr)TiO₃ thin films with different Ba content as determined by in situ photoelectron spectroscopy. For SrTiO₃ and BaTiO₃, also single crystal data are included. The numbers at the top indicate the Ba fraction on the *A*-site in %

compensation mechanism is determined by the formation enthalpies and charge transition levels of the involved defects. Therefore, adjusting material properties requires control of the formation enthalpies and charge transition levels of defects and dopants. Extensive and systematic studies of these quantities and their dependence on material composition will be necessary. Ideally, density functional theory should be able to describe the situation comprehensively. However, despite substantial progress in the field and very good agreement with selected experiments (see, e.g., [125, 126]), a quantitative description of defect properties in oxide electroceramics by density functional theory has not yet been achieved. Also, experimentally determined defect energy levels are rather scarce and restricted to few model substances, such as SrTiO₃ and BaTiO₃ [26, 127–129]. A simplification of the situation would be given if defect energy levels were transferable as in the case of transition metal defects in III-V semiconductors [82, 83]. Such an alignment has also been proposed for hydrogen impurities [24] and for oxygen vacancies [84] but without experimental verification. Recently, it has been demonstrated that the $Fe^{2+/3+}$ charge transition level in SrTiO₃ and BaTiO₃ is not aligned but close to the conduction band in the former and $\approx 0.8 eV$ below E_{CB} in the latter [26]. In contrast, the $Fe^{3+/4+}$ is $\approx 1 eV$ above the valence band in both materials [127, 130]. Density functional theory calculations have also revealed a difference of the respective levels in both materials [45] but not in agreement with experiments.

It is reasonable to conclude from the given descriptions that defect formation enthalpies and charge transition levels of defects depend on material composition and are not directly transferable from one compound to another. However, the dependencies open the possibility to control the

prevailing charge compensation mechanism by tailoring material composition, i.e. by adjusting the density of states in the valence and conduction band and thereby the charge transition levels of dopants. The latter includes adjusting E_{VB} and E_{CB}. Understanding these dependencies would therefore open the path for *Fermi level engineering* of oxide electroceramics.

For the implementation of Fermi level engineering, it is inevitable to understand the dependencies of defect energy levels. In order to emphasize the importance and the substantial lack of knowledge, known and anticipated energy levels of transition metal impurities in BaTiO₃ are provided in Fig. 14(a).

Experimentally determined defect energy levels (solid symbols) are available for the $4 + /3+$ and the $3 + /2+$ charge transitions of Mn and Fe [127]. Open symbols are anticipated dependencies. First of all, the $4 + /3+$ transition of Ti is expected to occur near the conduction band maximum, as donor doping or reduction results in high electronic conductivity [33], which corresponds to a Fermi level near E_{CB}. The $3 + /2+$ transition of Co in BiFeO₃ has been demonstrated to be about 1 eV lower in energy than the respective transition of Fe [54]. The same is assumed in Fig. 14(a). One should be aware, however, that the charge transition of isolated dopants, such as Fe in BaTiO₃, does not necessarily align with the valence change energy of Fe in BiFeO₃ [54]. It will therefore also be important to understand the dependence of the charge transition levels on the concentration of the species. While the energy level of Co is such that a 3+ valence is still possible, Ni more strongly prefers a 2+ valence. Its $3 + /2+$ transition is therefore expected to be lower in energy than that of Co. The two charge transition levels of Cu have recently

been identified for $CuGaO_2$ [133]. The energy levels may be transferred to $BaTiO_3$ using the energy band alignment between the materials, which places the Cu-containing compounds about 1.5 eV higher in energy [86]. Apart from Cu being a main constituent in $CuGaO_2$ and not a dilute dopant, the crystal structure and dielectric properties of the two materials differ widely. Eventually, the 2 + /0 transition of Zn and the 3 + /0 transition Ga have been included in Fig. 14. The increasing energy of these transitions is anticipated from the increasing stability of the compounds.

Although there are exceptions, the charge transition levels are expected to generally decrease with increasing order number within the 3d series. Taking into account the range of the Fermi energy in $BaTiO_3$, which is indicated by the green arrow at the right of Fig. 14, it should be possible to estimate the accessible oxidation states of the different 3d transition metals in dependence on Fermi energy. The range of Fermi energies is indicated in Fig. 14(b), which details data obtained at clean surfaces of several hundred polycrystalline (Ba,Sr)TiO_3 thin films with different Ba content. Also single crystal data are included for pure $SrTiO_3$ and $BaTiO_3$. For all compositions, the Fermi energies are at least 1.9 eV above E_{VB}. Fermi energies as low as $E_F - E_{VB} = 1.6$ eV have been observed at interfaces between $BaTiO_3$ and RuO_2 or NiO [131, 132]. In any case, all Fermi energies lie in the upper half of the energy gap. This is surprising, however, as lower Fermi energies are expected for Fe-doped $BaTiO_3$. With Na/Fe-codoped samples, even Fe^{5+} has been reported [27], which should correspond to a Fermi level of ≈ 0.5 eV above E_{VB} according to Fig. 14(a). Hole trapping, which is expected in $BaTiO_3$ on oxygen sites [134], may be one reason for the lower limit of the Fermi energy but still requires further confirmation. However, there is no direct experimental evidence for this so far and theory does currently not directly predict Fermi energy limitations.

5 The role of interfaces

In most cases, oxide electroceramic materials are used in the form of polycrystalline bulk ceramics. Grain boundaries but also surfaces and heterointerfaces (including electrode contacts) are inherent features of any device. Their impact on material properties is as important as that of the bulk. Surfaces determine sintering behavior and catalytic activity. Grain boundaries affect electric and dielectric properties, device stability but also microstructure evolution, and heterointerfaces are relevant for the mechanical and electrochemical stability and for electric contact properties. The influence of interfaces is largely related to the space-charge regions, which form in order to compensate the core charge of the interface.

5.1 Space-charge regions

In non-metallic materials, a common feature of interfaces is the presence of space-charge regions, which are connected to potential barriers. The design of potential barriers at grain boundaries is, for example, key to the non-linear current-voltage characteristic of varistors [15], the positive temperature coefficient of resistivity (PTCR) [16, 33, 135], and the basis for internal barrier layer capacitors [136]. Potential barriers do not only affect the transport of electronic charge carriers across or along grain boundaries, but also that of ionic charge carriers [137]. Accordingly, it poses a significant issue for any application that involves ionic conductors, as, for example, fuel and electrolytic cells, solid state batteries, gas separation membranes, and alike. This is related to the change of defect concentrations in the space-charge region [137, 138], resulting in enhanced or reduced ionic conductivities [139, 140]. The latter affects surface oxygen exchange [60, 139] and considerably slows down resistance degradation of acceptor-doped $BaTiO_3$ multilayer capacitors, a process related to oxygen ion migration [141, 142]. Modifications of surface acidity can affect surface exchange coefficients by many orders of magnitude, for example [143, 144].

The charged grain boundary core, which consists of the (few) atomic layer(s) required to match the crystal structures on both sides of the interface, are compensated by the charge accumulated in the space-charge region. In equilibrium, negatively or positively charged defects are accumulated or depleted in the space-charge region, depending on the sign of their charge relative to the interface core charge [145]. Free electrons and holes can establish equilibrium at any temperature. Certain ionic species, such as Li^+ or Na^+ in battery materials are sufficiently mobile at room temperature. For perovskites, such as $SrTiO_3$ and $BaTiO_3$, oxygen related defects are mobile from about 200 °C [130]. In most cases, cations require much higher temperatures to establish equilibrium distributions [35]. Only for few cases, such as Sn-doped In_2O_3, cations are already mobile from 300 °C [71, 146]. Temperatures high enough for cation diffusion are achieved during sample processing. Therefore, space-charge regions also constitute a driving force for cation accumulation/depletion [145]. These will affect microstructure evolution, which involves movement of grain boundaries. Grain boundary migration can be slowed down if the defects accumulated in the space-charge region cannot follow the migration of the boundary (solute drag) [58, 147, 148]. The combination of high-temperature materials processing and later application at lower temperatures results in a complex segregation state of grain boundaries: During processing, all point defects including cations equilibrate at the grain boundaries. During cooling, cationic concentration profiles are frozen in at some temperature and only anionic

and electronic defects further equilibrate, given the frozen concentration profile of the cations. Eventually, at very low temperatures, the anions become immobile as well, resulting in a complex non-equilibrium state of space charge and segregation. Typical applications fall either below (dielectrics) or within (electrolytes) the temperature range of anionic equilibration, but usually below the temperature of cationic equilibration (only exceptions are cathode materials for batteries). An example for a space-charge region and the related phenomena is detailed in Fig. 15.

While the basic features of grain boundaries in oxide electroceramics are known for some time, quantitative descriptions of the phenomena illustrated in Fig. 15 are barely available yet. Key issues would be the quantification of segregation effects, which determine the composition of the interface and thereby the charge of the interface and the related space-charge potential. As described above, segregation effects will depend on the Fermi level in the bulk and therefore on the doping species and concentration. The course of the electrostatic potential in the space-charge region will be affected by the defect energy levels of the dopants and by valence changes of the host species if the respective energy levels are crossing the Fermi energy in the space-charge region.

5.2 Interface charge

Literature distinguishes between electronic and ionic contributions to the interface charge. *Electronic contributions* originate from the distortion of chemical bonds and give rise
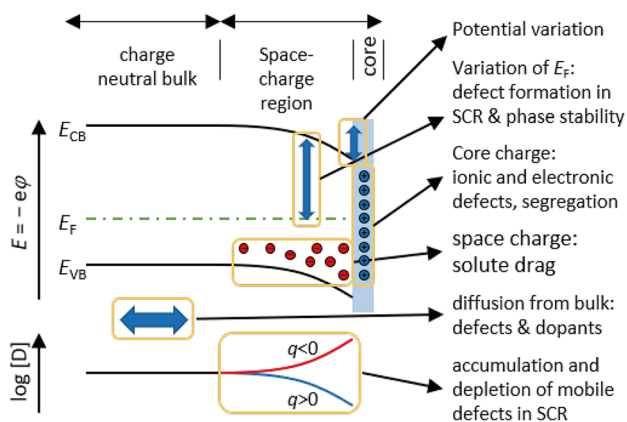

Fig. 15 A space-charge region (SCR) in an acceptor-doped material near an interface with a positive core charge. As indicated in the lower graph, mobile negatively charged electronic and ionic species are accumulated in the space-charge region while positive charges are depleted. Diffusion from the bulk also contributes to the segregation of defects and dopants to the interface core, which contribute to the core charge. The variation of the electrostatic potential ϕ in the space-charge region is important for material properties but also affects defect formation enthalpies and phase stability in the space-charge region

to a distribution of electronic states in the band gap resulting in trapped charge densities of up to 10^{14} cm^{-2}, corresponding to about 10 % of a monolayer [149–151]. Associated with this distribution of interface states is a charge neutrality level, E_{CNL}. The concept of the charge neutrality level can be rationalized by using a single dangling bond at a Si surface. The Si surface atom is electrically neutral if the dangling bond, whose energy is located within the energy gap of Si, is occupied with a single electron. Such an occupation is achieved when the Fermi energy coincides with the dangling bond energy. A higher (lower) Fermi energy results in a negative (positive) charge of the surface atom. As illustrated in Fig. 16(e), the real density of interface states, N_i is broadened due to the interaction between neighboring states. Still, the charge neutrality level will be close to the maximum of the density of states, resulting in a strong pinning of the Fermi energy next to E_{CNL}.

In ionic compounds, the distribution of electronic interface states is different due to the ionicity of the bond as illustrated in Fig. 16(c). Consequently, the electronic interface states can be separated into states with predominant cation and anion character, respectively, giving rise to electronic states being closer to the conduction and the valence band [152] as provided in Fig. 16(f). The charge neutrality level and the surface Fermi energy are typically located in between the cation- and the anion-related surface states, where the density of interface states is low. The cation (anion) interfaces states will therefore be mostly empty (filled) as in the bulk and the pinning of the Fermi energy will be weak. One important consequence of this behavior is the possibility to manufacture polycrystalline thin film solar cells with ionic semiconductors, such as Cu(In,Ga)Se$_2$ and CdTe. These can have efficiencies almost as high as those of single crystalline silicon [153], which is not possible with covalent Si and GaAs, where surfaces and grain boundaries are highly active recombination sites [154].

Ionic contributions to the interface core charge originate from the presence of ionic defects at the interface. These include vacancies, interstitials, and segregated impurities and dopants. Formation enthalpies of defects are typically lower at interfaces compared to the bulk. The concentration of defects is therefore often higher at the interface [66, 67]. On the other hand, impurities being insoluble in the bulk could be stable at interfaces [59, 155]. The resulting segregation of defects to the core has to be distinguished from the accumulation or depletion of defects in the space-charge region. A complete thermodynamic treatment, including segregation to grain boundaries and depletion in the space-charge region, has been developed for oxygen vacancies in acceptor-doped SrTiO$_3$ by De Souza [156].

The charge of ionic defects at interfaces is often assumed to be identical to that in the bulk. Cation and anion vacancies, for example, are expected to be negatively and
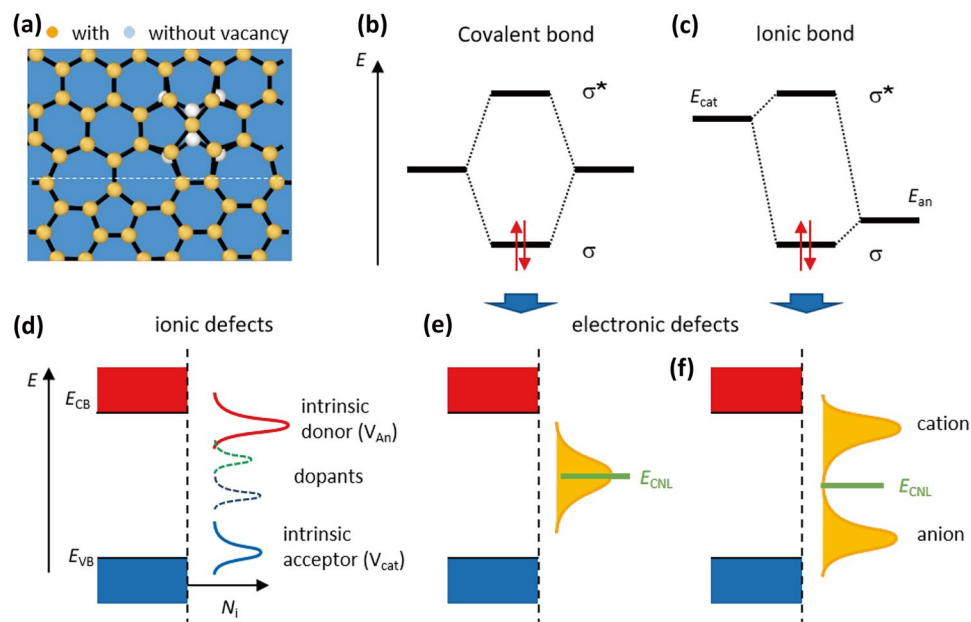
Fig. 16 (**a**) Structure of a grain boundary (dashed line) with and without a vacancy; (**b**) the distorted bonds at the grain boundary give rise to electronic defect states in the band gap; (**c**) Bonding scheme at an interface of a covalently and of an ionically bonded semiconductor; (**d**) Intrinsic ionic acceptor and donor defects (e.g., anion and cation vacancies V_{an} and V_{cat}) generate defect levels close to the band edges while dopants segregated to the grain boundary may have energy levels in the center of the gap; (**e**) For covalently bonded materials, the density of electronic interface states N_i is high in the center of the gap and near the charge neutrality level E_{CNL}; (**f**) For ionically bonded materials, N_i is split into a contribution from cations near the conduction band and a contribution from anions near the valence band

positively charged, regardless of the position of the Fermi energy at the interface. In an energy band diagram, this would correspond to electronic states being close to the valence band for the cation vacancy and close to the conduction band for the anion vacancy, as illustrated in Fig. 16(d), opposite to the electronic contribution to the density of interface states (Fig. 16(f)). The charge contributed by ionic defects to the interface core charge is also completely different from that of the electronic defects. As the Fermi energy at the interface will be, in most cases, located between the states of the cation and anion vacancies, ionic interfacial defects will indeed be charged. In contrast, electronic defects are only charged if the Fermi energy deviates from E_{CNL}.

The contributions of electronic and ionic defects to the interface charge are usually not considered together. While trapping of intrinsic ionic defects is sufficient to describe the formation of equilibrium space-charge regions in acceptor-doped $SrTiO_3$ [156], the electrical properties of ZnO varistors and of positive temperature coefficient resistors require a pinning of the potential barrier (Fermi energy) at the interface [33, 150]. Such a pinning cannot be provided by intrinsic ionic defects, as this requires energy levels at the pinning position. The pinning is thus most likely provided by segregation of dopants [33, 59], which can form deep electronic states at the grain boundary as depicted in

Fig. 16(d). Interactions of segregated dopants and intrinsic lattice defects may be further important for defining the density of states [157].

Tailoring the space-charge potential eventually entails controlling the density of states and thereby the charge at the grain boundary core. Most directly, the density of ionic defect states could be manipulated by the processing temperatures at which equilibrium of cation distributions can be established or not. Very often, processing of electroceramics contains sintering at high temperature and post-annealing at lower temperature in different atmosphere [15, 16, 158]. The optimization of properties by adjusting temperature profiles and annealing atmospheres is at least partially related to be control of the space-charge potential.

5.3 Surface properties

Surfaces exhibit contributions to the core charge from charged adsorbates, which can be easily exchanged with the environment in contrast to species at grain boundaries. This effect is the basis for gas sensors, where surface space-charge regions and hence the conductivity of the sensor material, typically a conductive oxide, such as SnO_2, are modified by adsorbed species [159]. However, while it is clear that adsorbates affect the Fermi energy
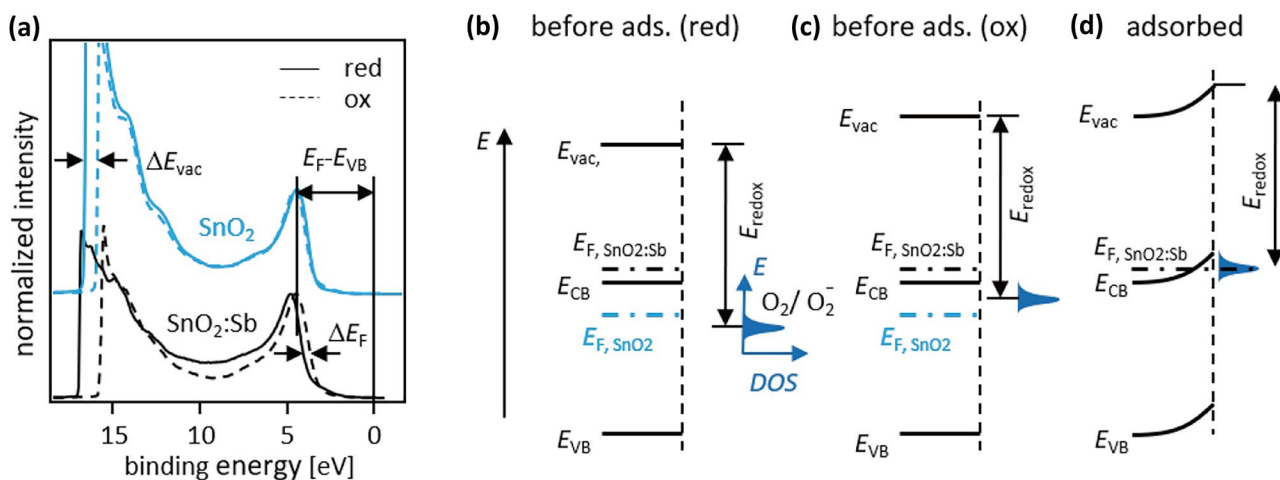
Fig. 17 (**a**) Valence band spectra of donor (Sb)-doped and undoped SnO_2 thin films with oxidized (Sn^{4+}) and reduced (Sn^{2+}) surface. The different binding energies of the valence bands near 5 eV correspond to different Fermi level positions. The variation in the secondary electron cutoff indicate a variation of the work function by a change of electron affinity, which is related to the different oxidation states of Sn; (**b**) Energy band diagram of the samples with reduced surfaces. Ionization of oxygen is possible for undoped and donor doped samples due to the higher E_F in SnO_2; (**c**) After oxidation of the surface, the vacuum level and the O_2/O_2^- redox level are shifted up in energy. Ionization of O_2 is then only possible for the donor-doped material with the higher Fermi energy; (**d**) Due to the negative surface charge of the adsorbed oxygen, a band bending develops at the SnO_2:Sb surface until the Fermi energy at the surface equals the O_2/O_2^- redox energy. Further adsorption of negatively charged O_2 is not possible

at the surface. it is also true that the Fermi energy at the surface affects adsorption and thereby catalytic behavior. This has already been proposed more than 50 years ago [160, 161].

An example for the influence of the Fermi energy on oxygen adsorption is illustrated in Fig. 17, featuring valence band photoelectron spectra of undoped and Sb-doped SnO_2 thin films, prepared under either reducing or oxidizing conditions. In order to bind oxygen molecules to the surface, electrons have to be transferred to the molecules to form O_2^-. Such a transfer is the first step for a complete oxygen reduction and an eventual incorporation of oxygen into a material [162]. The electron transfer is most facile for low work function (high Fermi energy). The work function can be changed by doping but also by changing the electron affinity ($E_{vac} - E_{CB}$). The latter varies by approximately 1 eV between oxidized and reduced SnO_2 surfaces [108]. Exposure to oxygen leads to an oxidation of the surface and a high electron affinity, after which electron transfer from undoped SnO_2 with a low E_F to O_2 molecules is no more possible. This effect, which is illustrated in Fig. 17(c), prevents oxygen incorporation into undoped SnO_2 [163]. In contrast, the Sb-doped samples, having a higher E_F, exhibit a surface band bending thus indicating a negative surface charge. Hence, charge transfer to O_2 is possible. The adsorption is, however, self-limited. The negative surface charge results in an upward band bending and therefore increases the work function until the O_2/O_2^- redox level coincides with the Fermi energy.

6 Relation to processing

6.1 Phase formation

Fermi level engineering has not only potential for improving material properties but may also contribute to advanced sample processing by understanding the influence of the Fermi energy and the defect energy levels. As a first example, we recall the influence of defect energy levels on the oxygen content in acceptor-doped $BaTiO_3$ [127, 128]. Figure 18(a) illustrates calculated oxygen vacancy concentrations in Fe- and Mn-doped $BaTiO_3$ using the defect energy levels given in Fig. 14. For the Fe-doped material, a plateau with $c(Fe) \approx 2 \cdot c(V_O^{\cdot\cdot})$ is clearly observed. This plateau is missing for Mn doping, for which the $3+/2+$ and the $4+/3+$ transition levels are much closer in energy. The respective Fermi energies do not differ much at the equilibration temperature but are noticeably different if the samples are quenched to 300 °C, freezing the oxygen vacancy concentration. This emphasizes that high temperature conductivity measurements, which are often used to study defect properties, are not sensitive to all defect energy levels, particularly not for those which are closer to the conduction band. In contrast, measurements at lower temperature, which are typically used in accelerated lifetime tests [141, 164], may be strongly affected by defect energy levels. The dependence of oxygen vacancy concentration on the defect energy level will also affect phase formation. In the case of $BaTiO_3$, Mn-doping is particularly stabilizing the hexagonal polytype, which is known to depend on the oxidation state of Mn [165].
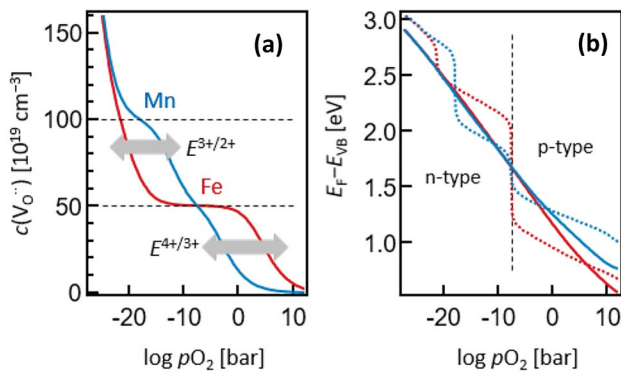
Fig. 18 (**a**) Oxygen vacancy concentration in $BaTiO_3$ in dependence on oxygen partial pressure for equilibration at $1100\,°C$, calculated using the defect energy levels for Fe and Mn from Fig. 14, which are taken from [127]. The doping concentration is taken as $10^{20}\ cm^{-3}$. The grey arrows indicate the influence of $3+/2+$ and of the $4+/3+$ transition levels; (**b**) Fermi level position as a function of oxygen partial pressure during equilibration at $1100\,°C$ (solid lines) and after quenching to $300\,°C$

A key ingredient of Fermi level engineering is the manipulation of the upper and the lower limits of the Fermi energy. One way to achieve this, is to introduce dopants with defect energy levels in order to confine the Fermi energy (see Section 4.3). An example for such a confinement is Co-doped $BiFeO_3$ [54]. As illustrated in Fig. 7, adsorption of water on $BiFeO_3$ results in an upward shift of the Fermi energy at the surface and consequently a reduction of Bi and Fe. The upward shift of E_F and the reduction can be suppressed by partially substituting Fe with Co. The $Co^{3+/2+}$ charge transition is $\approx 1\ eV$ lower in energy than the respective levels of Fe and Bi (see also Fig. 7). Hence, Co has to be reduced first if water is adsorbed on the surface. If the Co concentration is high enough, it will suppress the shift of the Fermi energy and thereby avoid the decomposition of the compound. In order to suppress the reduction of Bi and Fe, $10\,\%$ of the Fe were substituted by Co [54]. Such high concentrations often exceed the solubility limit of species (see Section 3.4). According to the description above, Fermi level engineering suggests two ways to increase the solubility limit: i) the introduced dopant must be isovalent to the substituted element. In the case of Co-doped $BiFeO_3$, this could be achieved by oxidizing synthesis conditions in order to maintain the Co^{3+} oxidation state; ii) a charged species can be compensated by an oppositely charged species. For acceptor-doped oxides, this can be accomplished by oxygen vacancies, requiring processing in an atmosphere with appropriate oxygen activity. For example, the tetravalent Ti in $BaTi_{1-x}Fe_x O_{3-x/2}$ is gradually replaced by trivalent Fe acceptor dopants. The charge compensation is then accomplished by half of an oxygen vacancy per Fe^{3+} species. By structural ordering of the oxygen vacancies and atomic relaxation, the perovskite structure becomes unstable for higher values of x. $BaTiO_{2.5}$

and $SrTiO_{2.5}$ crystallize in the monoclinic space group $P2_1/c$ and in the Brownmillerite structure, respectively [117, 166].

If the charge transition level of a certain dopant is beneficial for the properties, the concentration of the respective dopant may need to be increased beyond its solubility limit. This can be achieved by *codoping*, i.e. by the incorporation of the same amount of donors and acceptors. The compensating dopant can, but does not necessarily also have an influence on the properties. Its role may just be the increase of the concentration of the beneficial dopant species. These aspects may also be important for the formation of solid solutions of compounds with elements of different valences, for example $BaTiO_3$–$BiFeO_3$ or $BaTiO_3$–$(Na_{1/2}Bi_{1/2})TiO_3$. In principle, these can also be considered as codoped materials. In the first example, Bi_{Ba} is a donor and Fe_{Ti} an acceptor in $BaTiO_3$. In the second example, the Bi_{Ba} donors are charge compensated by Na_{Ba} acceptors. Donor and acceptor species in solid solutions could be incorporated in different concentrations due to a different volatility of species. This will eventually result in a net donor or acceptor doping and influence material properties and sintering behavior. The necessity for charge compensation in the case of net doping can also affect the site preference of species. It has, for example, been demonstrated by means of DFT calculations that trivalent Y and Mn in $BaTiO_3$ prefer to occupy either the Ba-sites as donors or the Ti-sites as acceptors depending on the Ba:Ti ratio [167].

The formation of secondary phases is sometimes difficult to avoid during solid state synthesis of oxide ceramic solid solutions [168, 169]. The solid oxide route typically involves carbonates and oxides. $CaZrO_3$ is, for example, synthesized using mixtures of $CaCO_3$ and ZrO_2. The enthalpy of formation of some oxides, such as ZrO_2, is very high and high processing temperatures are required for their reaction [168, 170]. The calcination of solid solution of, for example $NaNbO_3$ with $CaZrO_3$, may then start with a preferential solubility of Ca. This results in a higher Ca_{Na} donor concentration as compared to the Zr_{Nb} acceptor concentration. Consequently, the material is effectively donor doped. Eventually, the system has to react either by the formation of cation vacancies, by reduction of Nb^{5+} to Nb^{4+}, or by the segregation of the dopant, depending on the prevailing compensation mechanism. This does not mean that the targeted solid solution is not stable at all but just not with the obtained effective doping.

The phase instability by an inequivalent solubility of donor and acceptor species described in the previous paragraph is also expected to be an issue during synthesis of mixed anion compounds. In *oxyfluorides*, for example, starting from an oxide and substituting oxygen with fluorine corresponds to the introduction of F_O donor species. The topochemical reaction routes for the formation of oxy-fluorides are based on reacting an oxide together with a

fluorination agent [171, 172]. Various agents are known, among them gaseous F_2, XeF_2, NH_4F, CuF_2 and ZnF_2. Interestingly, the use of different reactants can, but may not necessarily lead to the same reaction product. This is related to the fact that fluorination reactions can be oxidative, substitutive or reductive, as indicated by the following reaction schemes for a perovskite type oxide with a divalent atom on the *A*-site and multivalent atom on the *B*-site:

Oxidative: An oxidative reaction leads to an increase of the oxidation state of a *B*-site cation. This is possible, if some of the *B*-site cations are present in a lower oxidation state than B^{4+}, which is charge compensated by oxygen vacancies (e.g., $BaFe^{4+}_{1-2x}Fe^{3+}_{2x}O_{3-x}$). Fluorine incorporation can then occur on one of the oxygen vacancy sites ($V_O^{\cdot\cdot} \rightarrow F_O^{\cdot}$). Thereby, an oxygen vacancy, which is a twofold donor, is replaced by fluorine, a single donor. This corresponds effectively to an acceptor doping and results in a lowering of the Fermi energy and consequently in the oxidation of the *B*-site cation, if this is the active compensation mechanism. The positive charge, which is missing after filling the oxygen vacancy with a fluorine ion, is then compensated by the oxidation of one of the *B*-site cations with a lower oxidation state. Therefore, an oxidative reaction requires the possibility to oxidize the *B*-site cation.

$$B_B' + V_O^{\cdot\cdot} + \frac{1}{2}F_2 \rightarrow B_B + F_O^{\cdot} \qquad (14)$$

Reductive: In this case, an oxygen atom is replaced by a fluorine atom. This corresponds to donor doping and results in an upward shift of the Fermi energy. The negative charge of the donor is compensated by a reduction of a *B*-site cation, if a valence change of the cation is the leading compensation mechanism. The reaction requires the possibility to lower the oxidation state of the *B*-site cation and, in addition, to remove oxygen from the sample:

$$B_B + O_O + \frac{1}{2}F_2 \rightarrow B_B' + F_O^{\cdot} + \frac{1}{2}O_2 \qquad (15)$$
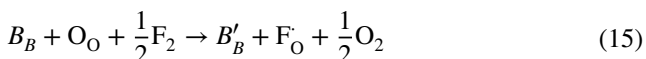
Substitutive: For substitutive reactions, the oxidation state of *B*-site cation will not change. In this case, one oxygen vacancy and one oxygen atom are replaced by two fluorine atoms, corresponding to a simultaneous donor ($O_O \rightarrow F_O^{\cdot}$) and acceptor doping ($V_O^{\cdot\cdot} \rightarrow F_O^{\cdot}$). Both are compensating each other and do not result in a shift of the Fermi energy. The reaction requires, however, that oxygen is being removed from the sample:

$$V_O^{\cdot\cdot} + O_O + F_2 \rightarrow 2F_O^{\cdot} + \frac{1}{2}O_2 \qquad (16)$$
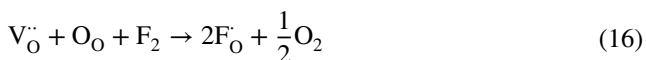
The formation of *oxynitrides* is typically performed by ammonolysis of oxide materials [78, 79]. The substitution of O with N corresponds to acceptor doping. Charge compensation may then be accomplished by formation of oxygen vacancies,

$$3O_O + N_2 \rightarrow 2N_O' + V_O^{\cdot\cdot} + \frac{3}{2}O_2, \qquad (17)$$
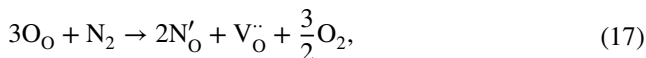
or alternatively by the oxidation of one of the cation species or holes in the valence. The latter two mechanisms may not available as in $BaTiO_3$, where neither Ba nor Ti can be oxidized. In such cases, oxygen vacancy formation must occur at the same rate as nitrogen incorporation. If this is kinetically not possible, the Fermi energy will approach either the upper or lower stability limit and formation of the desired phase will fail.

In general, the incorporation of large amounts of heterovalent species must be accompanied by charge compensation to avoid *overdoping* leading to the formation of unstable species. Any synthesis route must avoid high concentrations of donors or acceptors without charge compensation in order to avoid the formation of unstable intermediate species. A straightforward suggestion based on Fermi level engineering would be to avoid large changes of the Fermi energy, which implies to incorporate donor and acceptor species *simultaneously* as during codoping in cationic substitution and not *sequentially*. The respective effects on the Fermi energy are illustrated in Fig. 19.

6.2 Sintering and microstructure evolution

Sintering is driven by a reduction of free surface area and requires mass transport in the vicinity of the contact points between powder particles [168, 173]. There are various mass transfer mechanisms contributing to this process. Surface diffusion and evaporation/condensation do not contribute to densification and generally hinder sintering. The former is only relevant for materials with high vapor pressure. Relevant for densification are grain boundary and volume diffusion. As the concentration, and in some cases also the valence, of defects depends on the Fermi energy, both processes are directly affected by the Fermi energy, but in different ways. Volume diffusion refers to self-diffusion through the crystal lattice. In functional ceramics, the rate-controlling mechanism of this process is usually the diffusion of one of the cations. The diffusion coefficient of the cations increases with the concentration of cationic vacancies in the lattice. Cationic vacancies are negatively charged point defects that can result from a reduction or from donor doping, depending on the active charge compensation mechanism. The Fermi energy directly impacts, which charge compensation mechanism dominates for a given set of parameters, i.e., whether electronic or ionic defects are formed or whether valence changes or segregation prevails. Accordingly, beyond tweaking the functional properties, the
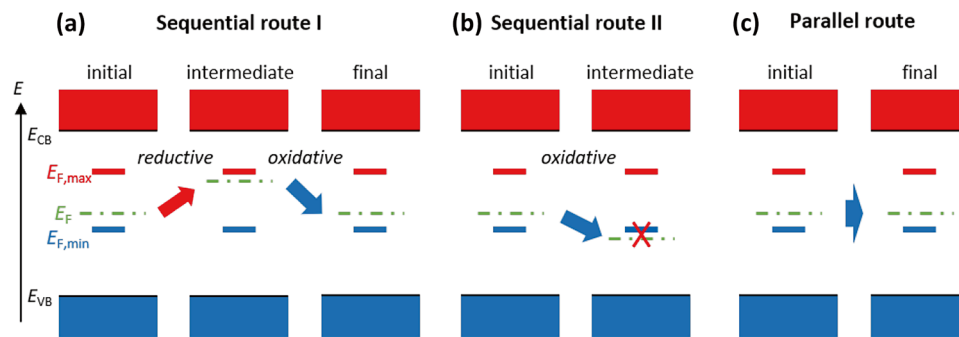
Fig. 19 Hypothetical illustration of the effect of different sequences of donor (reductive) and acceptor (oxidative) doping processes on the Fermi energy. For simplicity, changes of the stability limits, $E_{F,max}$ and $E_{F,min}$, and of the band edges are omitted. For the given example, sequential processing only works if the reductive treatment is carried out first (**a**), as the intermediate product is not stable when starting with the oxidative treatment (**b**). The instability can be avoided in any case by using a parallel route (**c**), in which donors and acceptors are substituted simultaneously

Fermi energy can be understood as a way to tailor volume diffusion coefficients for sintering.

In most materials, grain boundary migration is even more important for sintering. Here, the relationship between the Fermi energy and diffusion coefficients is more complex. In functional ceramics, grain boundaries involve space charge layers, which are well-known for their impact on electronic and ionic conductivities. A space charge layer involves a charged grain boundary core and a layer of accumulated or depleted point defects with opposite charge. Depending on the sign of the grain boundary core charge and the active charge compensation mechanism, the space charge layer can enhance grain boundary diffusion. Assuming a positive grain boundary core, negative point defects are accumulated in the space charge layer. This includes cationic vacancies if they are present in the bulk crystal. For these conditions, grain boundary diffusion is increased by the locally high concentration of cationic vacancies, resulting in a layer of fast diffusion along the network of grain boundaries. This effect was observed for $SrTiO_3$ [174].

Unfortunately, very little detailed knowledge is available on diffusion processes during sintering, particularly in relation to grain boundary migration. The available data are of limited quality and cannot be used for a quantitative description of sintering processes. For example, experimental volume diffusion data for alumina scatters over more than five orders of magnitude [168]. For alumina, at least some reports exist on grain boundary diffusion coefficients (see, e.g., [175]). Among functional ceramics, basic information is available for simple binary oxides, such as zirconia [176], and very little for perovskites [177]. The dependence of diffusion on the Fermi energy has not been investigated at all so far.

In addition to the anticipated relation between the Fermi energy and mass transport mechanisms as required for sintering, solute drag effects are important for microstructure evolution [140]. Solute drag is well-understood for metals [178] and refers to the diffusional drag of defects segregated to the grain boundaries. If defects ('solutes') segregate to the grain boundaries, their migration requires a diffusion of the defects along with grain boundary migration. This is in contrast to a grain boundary without segregation, where no such diffusion is required for grain boundary migration. Accordingly, grain boundary segregation generally results in inhibited grain growth if the segregated defects have a low diffusion coefficient in the hosting lattice.

Solute drag is well-investigated in various metallic systems [179]. However, very little is known on solute drag in functional ceramics. This is likely due to the more complex segregation behavior. Besides segregation to the grain boundary core as in metals, defects can accumulate (or deplete) in the space charge layer. The defects in the space charge layer can cause solute drag in the same way as those in the grain boundary core, if their diffusion coefficients are low [148]. Accordingly, the details of space-charge and segregation decide if solute drag occurs or not. The only functional perovskite-type oxide where this was analyzed is $SrTiO_3$ [147, 148, 180]. Here, the space-charge is known to depend on the oxygen partial pressure. In reducing atmosphere, very little space charge with very little cationic segregation occurs [156]. Consequently, only a minor solute drag occurs and grain growth is very fast [181]. In oxidizing atmosphere, the space-charge is much stronger and grain growth is significantly slower, resulting in a bimodal microstructure [182]. For other functional ceramics, only few reports investigated solute drag, e.g., in ceria [183], zirconia [184], yttria [185, 186], and $BaTiO_3$ [187].

Overall, solute drag is another aspect, where the Fermi energy is important for the processing of electroceramics, as it affects segregation to grain boundaries and accumulation/depletion of defects in the associated space-charge regions.

Note that Fermi level engineering can be used to tailor the functional properties of polycrystals. After best thermodynamic parameters were used to optimize diffusion during

sintering, the material can be re-annealed at a lower temperature using different thermodynamic parameters to optimize the conductivity. For example for strontium titanate, a strong space-charge with accumulated Sr vacancies results in good sintering [174]. However, a high ionic conductivity of the grain boundaries requires less space-charge, which can be obtained in reducing atmosphere [147, 156]. Such utilization of Fermi level engineering has not been investigated yet. However, $BaTiO_3$-based PTCR-materials are processed in such a way to obtain dense structures and optimized bulk and grain conductivity [16, 158].

6.3 Electrode interface stability

The Fermi energy at interfaces becomes important during co-firing of oxides with metallic electrodes, which is done in multilayer ceramic capacitors and actuators [188]. At the interface between the metallic electrode and the oxide, the Fermi energy in the oxide is determined by the Schottky barrier height of the contact. The barrier heights, and therefore the Fermi energy, can vary by more than one eV depending on oxygen activity [85]. In order to avoid an electrochemical reduction/oxidation of the oxide, the Fermi energy must remain within the stability limit of the compound. Such an electrochemical reduction has been directly observed, e.g., at interfaces between $BiFeO_3$ and Sn-doped In_2O_3 [54] and at interfaces between $Pb(Zr,Sn,Ti)O_3$ and Sn-doped In_2O_3 [189]. Due to such instabilities, the use of sintering in oxidizing conditions (air) may be required to sinter ceramic-metal stacks. This can prevent the desired use of non-noble metal electrode materials, such as Cu, which would oxidize and become non-conductive under such conditions [124]. It is noted that the work function of the ITO electrode used in the XPS experiments is $\approx 4.5\,eV$, which is comparable to that of many metallic electrode materials.

7 Summary and perspective

The concept of Fermi level engineering outlined in this contribution is the basis for semiconductor technology. The function of almost all semiconductor devices is determined by the spatial variation of the Fermi energy. Highly sophisticated devices are possible as the resulting properties can be accurately predicted for given material composition and processing. Such a prediction is not yet possible for electroceramic oxides, which, in many cases, are wide gap semiconductors. This is partially related to the richer defect chemistry of the involved materials, caused by lower defect formation energies in ionically bonded materials, the possibility for valence changes, segregation effects, and Fermi level-driven thermodynamic instabilities. On the other hand, a variety of interfaces are involved in the mostly polycrystalline oxide electroceramics. These are connected to ionic space-charge

regions, which strongly affect material properties but also their processing. Therefore, Fermi level engineering of oxide electroceramics is considerably more challenging than that of semiconductors. Nevertheless, the possibility to use the Fermi energy as the common descriptor for all involved defect formation processes constitutes a straightforward strategy to evaluate the dominant charge compensation mechanism. In principle, this opens the possibility to predict material properties for a given composition and processing of oxide electroceramics. Still, plenty of challenges have to be tackled. It is required to evaluate systematically the influence of sample composition (host materials and dopants)

- on the valence and conduction band edges,
- on the formation energies and charge transition levels of compensating ionic defects,
- on the formation energies and charge transition levels of different dopants and related segregation processes,
- on the possible valence changes of anions and cations,
- and on space-charge formation at interfaces.

Being able to directly obtain the Fermi energy is of utmost importance for this endeavor. Here, X-ray photoelectron spectroscopy has been demonstrated to be very useful as it provides simultaneously information on the chemical properties and the Fermi energy. The technique is particularly feasible for oxides, for which a wide variety of sample processing can be applied in vacuum systems. This in-situ processing is important as surface adsorbates from air exposure affect the Fermi level position. The available treatments of oxide surfaces feature a wide variation of oxygen activity, resulting in a large variation of the Fermi energy. With proper experiment and sample design, Fermi energy limits, defect energy levels, and interfacial space-charge regions can be quantified with XPS. Still, the experiments need further advancement to be applicable for a wide variation of materials and phenomena. Due to the importance of sample quality and reproducibility, a close collaboration with processing groups is mandatory. The combination with other defect characterization techniques, for example electron paramagnetic resonance, but also the whole toolbox of defect chemistry including AC and DC conductivity techniques, will be important and likely provide new insights into the properties of oxide electroceramics. Eventually, a deep understanding of Fermi level engineering can only be developed together with theory, as some aspects are and will not be accessible to experiment. It will be indispensable, however, to overcome current limitations of ab initio techniques in the quantification of defect parameters. To this end, the systematic experimental determination of defect properties will provide important benchmarks to further improve the theoretical descriptions.

Interfaces are particularly important for oxide electroceramics. This is mostly related to space-charge formation, which is directly affected by segregation processes. As

segregation phenomena are connected to the Fermi level and defect properties inside the grains, Fermi level engineering allows, in principle, to simultaneously control both bulk and interface properties. The connection of space-charge regions, phase stability, and defect concentrations to the Fermi energy can further help to modify or design new sample processing routes. These might enable synthesis of new or more reproducible materials.

Fermi level engineering is a way to think about materials development differently. It is still a long way to go until all the necessary ingredients of Fermi level engineering of oxide electroceramics are established. The challenges are manyfold, highly demanding, and require an intense collaboration between theory, sample processing, and characterization. It promises, however, to become an additional pathway to the development of materials for a plethora of important technologies and is therefore definitely worth the effort.

Declarations

Ethical approval Not applicable.

Involving human participants and/or animals Not applicable.

Informed consent Not applicable.

Competing interests The authors declare that they don't have any conflict or competing interest.

References

1. A.J. Moulson, J.M. Herbert, *Electroceramics*, 2nd edn. (John Wiley & Sons, Chichester, 2003)
2. N. Setter, R. Waser, Electroceramic Materials. Acta Mater. **48**(1), 151–178 (2000). https://doi.org/10.1016/S1359-6454(99)00293-1
3. R.C. Buchanan (ed.), *Ceramic Materials for Electronics* (Marcel Dekker Inc., New York 2004). https://doi.org/10.1201/9781315273242
4. H. Kishi, Y. Mizuno, H. Chazono, Base-Metal Electrode-Multilayer Ceramic Capacitors: Past, Present and Future Perspectives. Jpn. J. Appl. Phys. **42**(1R), 1–15 (2003). https://doi.org/10.1143/jjap.42.1
5. K. Hong, T.H. Lee, J.M. Suh, S.-H. Yoon, H.W. Jang, Perspectives and challenges in multilayer ceramic capacitors for next generation electronics. J. Mater. Chem. C **7**(32), 9782–9802 (2019). https://doi.org/10.1039/C9TC02921D
6. X. Zhu, W. Yang, *Mixed Conducting Ceramic Membranes* (Springer, Berlin 2017). https://doi.org/10.1007/978-3-662-53534-9
7. J.F. Scott, *Ferroelectric Memories* (Springer, Berlin 2000). https://doi.org/10.1007/978-3-662-04307-3
8. W. Heywang, K. Lubitz, W. Wersing (eds.), *Piezoelectricity: Evolution and Future of a Technology*. (Springer, Berlin 2008). https://doi.org/10.1007/978-3-540-68683-5
9. A. Kraytsberg, Y. Ein-Eli, Higher, Stronger, Better. A Review of 5 Volt Cathode Materials for Advanced Lithium-Ion Batteries. Adv. Energy Mater. **2**(8), 922–939 (2012). https://doi.org/10.1002/aenm.201200068
10. R. Waser, R. Dittmann, G. Staikov, K. Szot, Redox-Based Resistive Switching Memories - Nanoionic Mechanisms, Prospects, and Challenges. Adv. Mater. **21**(25–26), 2632–2663 (2009). https://doi.org/10.1002/adma.200900375
11. D.S. Ginley, H. Hosono, D.C. Paine (eds.), *Handbook of Transparent Conductors* (Springer, New York 2010). https://doi.org/10.1007/978-1-4419-1638-9
12. S.M. Sze, K.K. Ng, *Physics of Semiconductor Devices* (John Wiley & Sons, Hoboken 2007). https://doi.org/10.1002/0470068329
13. J. Maier, *Physical Chemistry of Ionic Materials* (Wiley-VCH, Weinheim 2004). https://doi.org/10.1002/0470020229
14. B. Jaffe, W.R. Cook, H. Jaffe, *Piezoelectric Ceramics* (Academic Press, London, 1971)
15. D.R. Clarke, Varistor Ceramics. J. Am. Ceram. Soc. **82**, 485–502 (1999). https://doi.org/10.1111/j.1151-2916.1999.tb01793.x
16. Y.L. Chen, S.F. Yang, PTCR effect in donor doped barium titanate: review of compositions, microstructures, processing and properties. Adv. Appl. Ceram. **110**, 257–269 (2011). https://doi.org/10.1179/1743676111Y.0000000001
17. J.B. Goodenough, Metallic oxides. Prog. Solid State Chem. **5**, 145–399 (1971). https://doi.org/10.1016/0079-6786(71)90018-5
18. J.B. Goodenough, Electronic and ionic transport properties and other physical aspects of perovskites. Rep. Prog. Phys. **67**(11), 1915 (2004). https://doi.org/10.1088/0034-4885/67/11/R01
19. A.P. Ramirez, Colossal magnetoresistance. J. Phys. Cond. Matter **9**, 8171–8199 (1997). https://doi.org/10.1088/0953-8984/9/39/005
20. C. Kittel, *Introduction to Solid State Physics* (Wiley, Hoboken, 2005)
21. H. Ibach, H. Lüth, *Solid-State Physics* (Springer, Dordrecht, 2009)
22. Y. Sun, S.E. Thompson, T. Nishida, *Strain Effect in Semiconductors* (Springer, New York, 2010)
23. P. Ágoston, K. Albe, Formation entropies of intrinsic point defects in cubic In_2O_3 from first-principles density functional theory calculations. Phys. Chem. Chem. Phys. **11**, 3226–3232 (2009). https://doi.org/10.1039/B900280D

24. C.G. Van de Walle, J. Neugebauer, Universal alignment of hydrogen levels in semiconductors, insulators and solutions. Nature **423**, 626–628 (2003). https://doi.org/10.1038/nature01665

25. P. Erhart, A. Klein, K. Albe, First-principles study on the structure and stability of oxygen related point defects in zinc oxide. Phys. Rev. B **72**, 085213 (2005). https://doi.org/10.1103/PhysRevB.72.085213

26. I. Suzuki, L. Gura, A. Klein, The energy level of the $Fe^{3+/2+}$-transition in $BaTiO_3$ and $SrTiO_3$ single crystals. Phys. Chem. Chem. Phys. **21**, 6238–6246 (2019). https://doi.org/10.1039/C8CP07872F

27. R. Scharfschwerdt, O.F. Schirmer, H. Hesse, D. Rytz, Fermi-level engineering of $BaTiO_3$ by alkali codoping: increasing the near-infrared absorption by rhodium. Appl. Phys. B **68**(5), 807–812 (1999). https://doi.org/10.1007/s003400050708

28. P. Ágoston, K. Albe, R.M. Nieminen, M.J. Puska, Intrinsic n-Type Behavior in Transparent Conducting Oxides: A Comparative Hybrid-Functional Study of In_2O_3, SnO_2, and ZnO. Phys. Rev. Lett. **103**, 245501 (2009). https://doi.org/10.1103/PhysRevLett.103.245501

29. P. Wendel, D. Dietz, J. Deuermeier, A. Klein, Reversible Barrier Switching of ZnO/RuO_2 Schottky Diodes. Materials **14**(10), 2678 (2021)

30. C. Freysoldt, B. Grabowski, T. Hickel, J. Neugebauer, G. Kresse, A. Janotti, C.G.V. de Walle, First-principles calculations for point defects in solids. Rev. Mod. Phys. **86**(1), 253–305 (2014). https://doi.org/10.1103/RevModPhys.86.253

31. S.B. Zhang, J.E. Northrup, Chemical potential dependence of defect formation energies in GaAs: Application to Ga self-diffusion. Phys. Rev. Lett. **67**(17), 2339–2342 (1991). https://doi.org/10.1103/PhysRevLett.67.2339

32. O. Saburi, Properties of Semiconductive Barium Titanates. J. Phys. Soc. Jpn. **14**, 1159–1174 (1959). https://doi.org/10.1143/JPSJ.14.1159

33. W. Preis, W. Sitte, Electrical properties of grain boundaries in interfacially controlled functional ceramics. J. Electroceram. **34**(2), 185–206 (2015). https://doi.org/10.1007/s10832-014-9972-7

34. J. Daniels, K.H. Härdtl, R. Wernicke, The PTC effect of barium titanate. Philips Tech. Rev. **38**, 73 (1979)

35. R. Meyer, A.F. Zurhelle, R.A. De Souza, R. Waser, F. Gunkel, Dynamics of the metal-insulator transition of donor-doped $SrTiO_3$. Phys. Rev. B **94**(11), 115408 (2016). https://doi.org/10.1103/PhysRevB.94.115408

36. S.B. Zhang, S.-H. Wei, A. Zunger, A phenomenological model for systemization and prediction of doping limits in II-VI and I-III-VI$_2$ compounds. J. Appl. Phys. **83**(6), 3192–3196 (1998). https://doi.org/10.1063/1.367120

37. W. Walukiewicz, Intrinsic limitations to the doping of wide-gap semiconductors. Physica B **302–303**(1), 123–134 (2001). https://doi.org/10.1016/S0921-4526(01)00417-3

38. J. Robertson, S.J. Clark, Limits to doping in oxides. Phys. Rev. B **83**(7), 075205 (2011). https://doi.org/10.1103/PhysRevB.83.075205

39. J.A. van Vechten, J.D. Zook, R.D. Horning, B. Goldenberg, Defeating compensation in wide gap semiconductors by growing in H that is removed by low temperature de-ionizing radiation. Jpn. J. Appl. Phys. **31**(Part I, No. 11), 3662–3663 (1992). https://doi.org/10.1143/JJAP.31.3662

40. M.I. Morozov, D. Damjanovic, Charge migration in $Pb(Zr, Ti)O_3$ ceramics and its relation to ageing, hardening, and softening. J. Appl. Phys. **107**, 034106 (2010). https://doi.org/10.1063/1.3284954

41. C. Slouka, T. Kainz, E. Navickas, G. Walch, H. Hutter, K. Reichmann, J. Fleig, The Effect of Acceptor and Donor Doping on Oxygen Vacancy Concentrations in Lead Zirconate Titanate (PZT). Materials **9**(11) (2016). https://doi.org/10.3390/ma9110945

42. S.-H. Yoon, C.A. Randall, K.-H. Hur, Difference between resistance degradation of fixed valence acceptor (Mg) and variable valence acceptor (Mn)-doped $BaTiO_3$ ceramics. J. Appl. Phys. **108**(6), 064101 (2010). https://doi.org/10.1063/1.3480992

43. P. Ágoston, C. Körber, A. Klein, M.J. Puska, R.M. Nieminen, K. Albe, Limits for n-type doping in In_2O_3 and SnO_2: A theoretical approach by first-principles calculations using hybrid-functional methodology. J. Appl. Phys. **108**(5), 053511 (2010). https://doi.org/10.1063/1.3467780

44. K. Ellmer, Past achievements and future challenges in the development of optically transparent electrodes. Nature Photonics **6**, 809–817 (2012). https://doi.org/10.1038/NPHOTON.2012.282

45. J.N. Baker, P.C. Bowes, J.S. Harris, D.L. Irving, Mechanisms governing metal vacancy formation in $BaTiO_3$ and $SrTiO_3$. J. Appl. Phys. **124**(11), 114101 (2018). https://doi.org/10.1063/1.5044746

46. A.M. Stoneham, J. Gavartin, A.L. Shluger, A.V. Kimmel, D. Muños Ramo, H.M. Rønnow, G. Aeppli, C. Renner, Trapping, self-trapping and the polaron family. J. Phys. Cond. Matter **19**, 255208 (2007). https://doi.org/10.1088/0953-8984/19/25/255208

47. S. Chen, L.-W. Wang, Thermodynamic Oxidation and Reduction Potentials of Photocatalytic Semiconductors in Aqueous Solution. Chem. Mater. **24**(18), 3659–3666 (2012). https://doi.org/10.1021/cm302533s

48. J.W. Schultze, M.M. Lohrengel, Stability, reactivity and breakdown of passive films. Problems of recent and future research. Electrochimica Acta **45**, 2499–2513 (2000). https://doi.org/10.1016/S0013-4686(00)00347-9

49. J. Mizusaki, T. Sasamoto, W.R. Cannon, H.K. Bowen, Electronic Conductivity, Seebeck Coefficient, and Defect Structure of $La_{1-x}Sr_xFeO_3$ ($x = 0.1, 0.25$). J. Am. Ceram. Soc. **66**(4), 247–252 (1983). https://doi.org/10.1111/j.1151-2916.1983.tb15707.x

50. O.F. Schirmer, M. Imlau, C. Merschjann, B. Schoke, Electron small polarons and bipolarons in $LiNbO_3$. J. Phys.: Cond. Matter **21**(12), 123201 (2009). https://doi.org/10.1088/0953-8984/21/12/123201

51. J. Robertson, W.L. Warren, B.A. Tuttle, Band states and shallow hole traps in $Pb(Zr, Ti)O_3$ ferroelectrics. J. Appl. Phys. **77**(8), 3975–3980 (1995). https://doi.org/10.1063/1.358580

52. C. Lohaus, A. Klein, W. Jaegermann, Limitation of Fermi level shifts by polaron defect states in hematite photoelectrodes. Nature Commun. **9**, 4309 (2018). https://doi.org/10.1038/s41467-018-06838-2

53. J. Lee, S. Han, Thermodynamics of native point defects in a-Fe_2O_3: an ab initio study. Phys. Chem. Chem. Phys. **15**(43), 18906–18914 (2013). https://doi.org/10.1039/C3CP53311E

54. N.S. Bein, P. Machado, M. Coll, F. Chen, M. Makarovic, T. Rojac, A. Klein, Electrochemical Reduction of Undoped and Cobalt-Doped $BiFeO_3$ Induced by Water Exposure: Quantitative Determination of Reduction Potentials and Defect Energy Levels Using Photoelectron Spectroscopy. J. Phys. Chem. Lett. **10**, 7071–7076 (2019). https://doi.org/10.1021/acs.jpclett.9b02706

55. Y. Hermans, A. Klein, S. Murcia-López, W. Jaegermann, $BiVO_4$ Surface Reduction upon Water Exposure. ACS Energy Lett. **4**(10), 2522–2528 (2019). https://doi.org/10.1021/acsenergylett.9b01667

56. A.C. Caballero, J.F. Fernández, C. Moure, P. Durán, Y.-M. Chiang, Grain Growth Control and Dopant Distribution in ZnO-Doped $BaTiO_3$. J. Am. Ceram. Soc. **81**(4), 939–944 (1998). https://doi.org/10.1111/j.1151-2916.1998.tb02430.x

57. B. Malič, J. Koruza, J. Hreščak, J. Bernard, K. Wang, J.G. Fisher, A. Benčan, Sintering of Lead-Free Piezoelectric Sodium Potassium Niobate Ceramics. Materials **8**(12), 8117–8146 (2015). https://doi.org/10.3390/ma8125449

58. J.W. Cahn, The impurity-drag effect in grain boundary motion. Acta Metallurgica **10**(9), 789–798 (1962). https://doi.org/10.1016/0001-6160(62)90092-5

59. Y. Sato, T. Yamamoto, Y. Ikuhara, Atomic Structures and Electrical Properties of ZnO Grain Boundaries. J. Am. Ceram. Soc. **90**(2), 337–357 (2007). https://doi.org/10.1111/j.1551-2916.2006.01481.x

60. R.A. De Souza, Oxygen Diffusion in $SrTiO_3$ and Related Perovskite Oxides. Adv. Funct. Mater. **25**(40), 6326–6342 (2015). https://doi.org/10.1002/adfm.201500827

61. O. Kwon, S. Joo, S. Choi, S. Sengodan, G. Kim, Review on exsolution and its driving forces in perovskites. J. Phys. Energy **2**(3), 032001 (2020). https://doi.org/10.1088/2515-7655/ab8c1f

62. N.H. Perry, T. Ishihara, Roles of Bulk and Surface Chemistry in the Oxygen Exchange Kinetics and Related Properties of Mixed Conducting Perovskite Oxide Electrodes. Materials **9**(10), 858 (2016). https://doi.org/10.3390/ma9100858

63. A.K. Opitz, C. Rameshan, M. Kubicek, G.M. Rupp, A. Nenning, T. Götsch, R. Blume, M. Hävecker, A. Knop-Gericke, G. Rupprechter, B. Klötzer, J. Fleig, The Chemical Evolution of the $La_{0.6}Sr_{0.4}CoO_{3-\delta}$ Surface Under SOFC Operating Conditions and Its Implications for Electrochemical Oxygen Exchange Activity. Topics in Catalysis **61**(20), 2129–2141 (2018). https://doi.org/10.1007/s11244-018-1068-1

64. Y. Chen, W. Jung, Z.H. Cai, J.J. Kim, H.L. Tuller, B. Yildiz, Impact of Sr segregation on the electronic structure and oxygen reduction activity of $SrTi_{1-x}Fe_xO_3$ surfaces. Energy Environ. Sci. **5**(7), 7979–7988 (2012). https://doi.org/10.1039/c2ee21463f

65. Z. Cai, M. Kubicek, J. Fleig, B. Yildiz, Chemical Heterogeneities on $La_{0.6}Sr_{0.4}CoO_{3-\delta}$ Thin Films–Correlations to Cathode Surface Activity and Stability. Chem. Mater. **24**(6), 1116–1127 (2012). https://doi.org/10.1021/cm203501u

66. S. Lany, A. Zakutayev, T.O. Mason, J.F. Wager, K.R. Poeppelmeier, J.D. Perkins, J.J. Berry, D.S. Ginley, A. Zunger, Surface Origin of High Conductivities in Undoped In_2O_3 Thin Films. Phys. Rev. Lett. **108**, 016802 (2012). https://doi.org/10.1103/PhysRevLett.108.016802

67. A. Walsh, Surface oxygen vacancy origin of electron accumulation in indium oxide. Appl. Phys. Lett. **98**(26), 261910 (2011). https://doi.org/10.1063/1.3604811

68. M.F. Yan, R.M. Cannon, H.K. Bowen, Space charge, elastic field, and dipole contributions to equilibrium solute segregation at interfaces. J. Appl. Phys. **54**(2), 764–778 (1983). https://doi.org/10.1063/1.332035

69. W. Lee, J.W. Han, Y. Chen, Z. Cai, B. Yildiz, Cation Size Mismatch and Charge Interactions Drive Dopant Segregation at the Surfaces of Manganite Perovskites. J. Am. Chem. Soc. **135**(21), 7909–7925 (2013). https://doi.org/10.1021/ja3125349

70. M.V. Frischbier, H.F. Wardenga, M. Weidner, O. Bierwagen, J. Jia, Y. Shigesato, A. Klein, Influence of dopant species and concentration on grain boundary scattering in degenerately doped In_2O_3 thin films. Thin Solid Films **614**, 62–68 (2016). https://doi.org/10.1016/j.tsf.2016.03.022

71. Y. Gassenbauer, R. Schafranek, A. Klein, S. Zafeiratos, M. Hävecker, A. Knop-Gericke, R. Schlögl, Surface states, surface potentials and segregation at surfaces of tin-doped In_2O_3. Phys. Rev. B **73**(24), 245312 (2006). https://doi.org/10.1103/PhysRevB.73.245312

72. S. Lany, A. Zunger, Dopability, Intrinsic Conductivity, and Nonstoichiometry of Transparent Conducting Oxides. Phys. Rev. Lett. **98**(4), 045501 (2007). https://doi.org/10.1103/PhysRevLett.98.045501

73. C. Agashe, O. Kluth, J. Hüpkes, U. Zastrow, B. Rech, M. Wuttig, Efforts to improve carrier mobility in radio frequency sputtered aluminum doped zinc oxide films. J. Appl. Phys. **95**(4), 1911–1917 (2004). https://doi.org/10.1063/1.1641524

74. N. Bein, B. Kmet, T. Rojac, A.B. Golob, B. Malic, J. Moxter, T. Schneider, L. Fulanovic, M. Azadeh, T. Frömling, S. Egert, H. Wang, P. van Aken, J. Schwarzkopf, A. Klein, Fermi Energy, Electrical Conductivity, and the Energy Gap of $NaNbO_3$. Phys. Rev. Mater. **6**, 084404 (2022). https://doi.org/10.1103/PhysRevMaterials.6.084404

75. A. Walsh, J.L.F.D. Silva, S.-H. Wei, C. Körber, A. Klein, L.F.J. Piper, A. DeMasi, K.E. Smith, G. Panaccione, P. Torelli, D.J. Payne, A. Bourlange, R.G. Egdell, The nature of the bandgap in In_2O_3 revealed by first-principles calculations and X-ray spectroscopy. Phys. Rev. Lett. **100**, 167402 (2008). https://doi.org/10.1103/PhysRevLett.100.167402

76. X. Nie, S.-H. Wei, S.B. Zhang, Bipolar Doping and Band-Gap Anomalies in Delafossite Transparent Conductive Oxides. Phys. Rev. Lett. **88**, 066405 (2002). https://doi.org/10.1103/PhysRevLett.88.066405

77. A. Fujishima, X. Zhang, D.A. Tryk, TiO_2 photocatalysis and related surface phenomena. Surf. Sci. Rep. **63**(12), 515–582 (2008). https://doi.org/10.1016/j.surfrep.2008.10.001

78. S.G. Ebbinghaus, H.-P. Abicht, R. Dronskowski, T. Müller, A. Reller, A. Weidenkaff, Perovskite-related oxynitrides - Recent developments in synthesis, characterisation and investigations of physical properties. Prog. Solid State Chem. **37**(2), 173–205 (2009). https://doi.org/10.1016/j.progsolidstchem.2009.11.003

79. A. Fuertes, Synthetic approaches in oxynitride chemistry. Prog. Solid State Chem. **51**, 63–70 (2018). https://doi.org/10.1016/j.progsolidstchem.2017.11.001

80. W.A. Harrison, *Electronic Structure and the Properties of Solids* (Dover Publications, New York, 1989)

81. W.A. Harrison, J. Tersoff, Tight-binding theory of heterojunction band lineups and interface dipoles. J. Vac. Sci. Technol. B **4**(4), 1068–1073 (1986). https://doi.org/10.1116/1.583544

82. A. Zunger, Theory of 3d Transition Atom Impurities in Semiconductors. Ann. Rev. Mater. Sci. **15**(1), 411–453 (1985). https://doi.org/10.1146/annurev.ms.15.080185.002211

83. J.M. Langer, C. Delerue, M. Lannoo, H. Heinrich, Transition-metal impurities in semiconductors and heterojunction band lineups. Phys. Rev. B **38**(11), 7723–7739 (1988). https://doi.org/10.1103/PhysRevB.38.7723

84. C. Linderälv, A. Lindman, P. Erhart, A Unifying Perspective on Oxygen Vacancies in Wide Band Gap Oxides. J. Phys. Chem. Lett. **9**(1), 222–228 (2018). https://doi.org/10.1021/acs.jpclett.7b03028

85. A. Klein, Interface Properties of Dielectric Oxides. J. Am. Ceram. Soc. **99**, 369–387 (2016). https://doi.org/10.1111/jace.14074

86. S. Li, F. Chen, R. Schafranek, T.J.M. Bayer, K. Rachut, A. Fuchs, S. Siol, M. Weidner, M. Hohmann, V. Pfeifer, J. Morasch, C. Ghinea, E. Arveux, R. Günzler, J. Gassmann, C. Körber, Y. Gassenbauer, F. Säuberlich, G.V. Rao, S. Payan, M. Maglione, C. Chirila, L. Pintilie, L. Jia, K. Ellmer, K. Naderer, K. Reichmann, U. Böttger, S. Schmelzer, R.C. Frunza, H. Uršič, B. Malič, W.-B. Wu, P. Erhart, A. Klein, Intrinsic energy band alignment of functional oxides. Phys. Stat. Sol. (RRL) **8**, 571–576 (2014). https://doi.org/10.1002/pssr.201409034

87. J.O. McCaldin, T.C. McGill, C.A. Mead, Correlation for III-V and II-VI Semiconductors of the Au Schottky Barrier Energy with Anion Electronegativity. Phys. Rev. Lett. **36**(1), 56–58 (1976). https://doi.org/10.1103/PhysRevLett.36.56

88. J. Tersoff, Theory of semiconductor heterojunction: The role of quantum dipoles. Phys. Rev. B **30**(8), 4874–4877 (1984). https://doi.org/10.1103/PhysRevB.30.4874

89. J. Tersoff, Schottky barrier heights and the continuum of gap states. Phys. Rev. Lett. **52**(6), 465–468 (1984). https://doi.org/10.1103/PhysRevLett.52.465

90. S. Kurtin, T.C. McGill, C.A. Mead, Fundamental transition in the electronic nature of solids. Phys. Rev. Lett. **22**, 1433–1436 (1969). https://doi.org/10.1103/PhysRevLett.22.1433

91. S. Siol, J.C. Hellmann, S.D. Tilley, M. Graetzel, J. Morasch, J. Deuermeier, W. Jaegermann, A. Klein, Band Alignment Engineering at Cu_2O/ZnO Heterointerfaces. ACS Appl. Mater. Interfaces **8**, 21824–21831 (2016). https://doi.org/10.1021/acsami.6b07325

92. V. Pfeifer, P. Erhart, S. Li, K. Rachut, J. Morasch, J. Brötz, P. Reckers, T. Mayer, S. Rühle, A. Zaban, I.M. Serø, J. Bisquert, W. Jaegermann, A. Klein, Energy Band Alignment Between Anatase and Rutile TiO_2. J. Phys. Chem. Lett. **4**, 4182–4187 (2013). https://doi.org/10.1021/jz402165b

93. R. Schafranek, S. Li, F. Chen, W. Wu, A. Klein, PbTiO$_3$/SrTiO$_3$ interface: Energy band alignment and its relation to the limits of Fermi level variation. Phys. Rev. B **84**(4), 045317 (2011). https://doi.org/10.1103/PhysRevB.84.045317

94. S. Li, J. Morasch, A. Klein, C. Chirila, L. Pintilie, L. Jia, K. Ellmer, M. Naderer, K. Reichmann, M. Gröting, K. Albe, Influence of orbital contributions to valence band alignment of Bi$_2$O$_3$, Fe$_2$O$_3$, BiFeO$_3$, and Bi$_{0.5}$Na$_{0.5}$TiO$_3$. Phys. Rev. B **88**, 045428 (2013). https://doi.org/10.1103/PhysRevB.88.045428

95. Y. Hermans, A. Klein, K. Ellmer, R. van de Krol, T. Toupance, W. Jaegermann, Energy Band Alignment of BiVO$_4$ from Photoelectron Spectroscopy of Solid-state Interfaces. J. Phys. Chem. C **122**, 20861–20870 (2018). https://doi.org/10.1021/acs.jpcc.8b06241

96. Y. Ogo, H. Hiramatsu, K. Nomura, H. Yanagi, T. Kamiya, M. Hirano, H. Hosono, p-channel thin-film transistor using p-type oxide semiconductor. SnO. Appl. Phys. Lett. **93**, 032113 (2008). https://doi.org/10.1063/1.2964197

97. A. Bhatia, G. Hautier, T. Nilgianskul, A. Miglio, J. Sun, H.J. Kim, K.H. Kim, S. Chen, G.-M. Rignanese, X. Gonze, J. Suntivich, High-Mobility Bismuth-based Transparent p-Type Oxide from High-Throughput Material Screening. Chem. Mater. **28**(1), 30–34 (2016). https://doi.org/10.1021/acs.chemmater.5b03794

98. S.B. Zhang, S.-H. Wei, A. Zunger, Microscopic Origin of the Phenomenological Equilibrium Doping Limit Rule in n-Type III-V Semiconductors. Phys. Rev. Lett. **84**(6), 1232–1235 (2000). https://doi.org/10.1103/PhysRevLett.84.1232

99. H. Kawazoe, M. Yasukawa, H. Hyodo, M. Kurita, H. Yanagi, H. Hosono, P-type electrical conduction in transparent thin films of CuAlO$_2$. Nature **389**, 939–942 (1997). https://doi.org/10.1038/40087

100. A. Kudo, H. Yanagi, H. Hosono, H. Kawazoe, SrCu$_2$O$_2$: A p-type conductive oxide with wide band gap. Appl. Phys. Lett. **73**(2), 220–222 (1998). https://doi.org/10.1063/1.121761

101. B.K. Meyer, A. Polity, D. Reppin, M. Becker, P. Hering, P.J. Klar, T. Sander, C. Reindl, J. Benz, M. Eickhoff, C. Heiliger, M. Heinemann, J. Bläsing, A. Krost, S. Shokovets, C. Müller, C. Ronning, Binary copper oxide semiconductors: From materials towards devices. Phys. Stat. Sol. (B) **249**, 1487–1509 (2012). https://doi.org/10.1002/pssb.201248128

102. F.E. Oropeza, N.Y. Dzade, A. Pons-Martí, Z. Yang, K.H.L. Zhang, N.H. de Leeuw, E.J.M. Hensen, J.P. Hofmann, Electronic Structure and Interface Energetics of CuBi$_2$O$_4$ Photoelectrodes. J. Phys. Chem. C **124**, 22416–22425 (2020). https://doi.org/10.1021/acs.jpcc.0c08455

103. Y. Hermans, A. Klein, H.P. Sarker, M.N. Huda, H. Junge, T. Toupance, W. Jaegermann, Pinning of the Fermi Level in CuFeO$_2$ by Polaron Formation Limiting the Photovoltage for Photochemical Water Splitting. Adv. Funct. Mater. **30**(10), 1910432 (2020). https://doi.org/10.1002/adfm.201910432

104. F. Capasso, G. Margaritondo (eds.), *Heterojunction*, vol. Discontinuities (North-Holland, Amsterdam, 1987)

105. J.R. Waldrop, R.W. Grant, S.P. Kowalczyk, E.A. Kraut, Measurement of semiconductor heterojunction band discontinuities by X-ray photoemission spectroscopy. J. Vac. Sci. Technol. A **3**(3), 835–841 (1985). https://doi.org/10.1116/1.573326

106. A. Klein, Energy band alignment at interfaces of semiconducting oxides: A review of experimental determination using photoelectron spectroscopy and comparison with theoretical predictions by the electron affinity rule, charge neutrality levels, and the common anion rule. Thin Solid Films **520**, 3721–3728 (2012). https://doi.org/10.1016/j.tsf.2011.10.055

107. M.T. Greiner, L. Chai, M.G. Helander, W.-M. Tang, Z.-H. Lu, Transition Metal Oxide Work Functions: The Influence of Cation Oxidation State and Oxygen Vacancies. Adv. Funct. Mater. **22**(21), 4557–4568 (2012). https://doi.org/10.1002/adfm.201200615

108. A. Klein, C. Körber, A. Wachau, F. Säuberlich, Y. Gassenbauer, S.P. Harvey, D.E. Proffit, T.O. Mason, Transparent Conducting Oxides for Photovoltaics: Manipulation of Fermi Level, Work Function, and Energy Band Alignment. Materials **3**, 4892–4914 (2010). https://doi.org/10.3390/ma3114892

109. C. Noguera, Polar oxide surfaces. J. Phys. Cond. Matter **12**(31), 367–410 (2000). https://doi.org/10.1088/0953-8984/12/31/201

110. S. Kashiwaya, J. Morasch, V. Streibel, T. Toupance, W. Jaegermann, A. Klein, The work function of TiO$_2$. Surfaces **1**, 73–89 (2018). https://doi.org/10.3390/surfaces1010007

111. M. Grätzel, Photoelectrochemical cells. Nature **414**, 338 (2001). https://doi.org/10.1038/35104607

112. R. van de Krol, M. Grätzel (eds.), *Photoelectrochemical Hydrogen Production* (Springer, Boston, MA 2012). https://doi.org/10.1007/978-1-4614-1380-6

113. S. Trasatti, The absolute electrode potential: an explanatory note (Recommendations 1986). J. Electroanal. Chem. **209**, 417–428 (1986). https://doi.org/10.1016/0022-0728(86)80570-8

114. P. Deák, B.L. Aradi, T. Frauenheim, Band Lineup and Charge Carrier Separation in Mixed Rutile-Anatase Systems. J. Phys. Chem. C **115**, 3443–3446 (2011). https://doi.org/10.1021/jp1115492

115. D.O. Scanlon, C.W. Dunnill, J. Buckeridge, S.A. Shevlin, A.J. Logsdail, S.M. Woodley, C.R.A. Catlow, M.J. Powell, R.G. Palgrave, I.P. Parkin, G.W. Watson, T.W. Keal, P. Sherwood, A. Walsh, A.A. Sokol, Band alignment of rutile and anatase TiO$_2$. Nature Mater. **12**, 798 (2013). https://doi.org/10.1038/nmat3697

116. M. Imada, A. Fujimori, Y. Tokura, Metal-insulator transitions. Rev. Mod. Phys. **70**(4), 1039–1263 (1998). https://doi.org/10.1103/RevModPhys.70.1039

117. O. Clemens, M. Gröting, R. Witte, J.M. Perez-Mato, C. Loho, F.J. Berry, R. Kruk, K.S. Knight, A.J. Wright, H. Hahn, P.R. Slater, Crystallographic and Magnetic Structure of the Perovskite-Type Compound BaFeO$_{2.5}$: Unrivaled Complexity in Oxygen Vacancy Ordering. Inorg. Chem. **53**(12), 5911–5921 (2014). https://doi.org/10.1021/ic402988y

118. M.F. Hoedl, D. Gryaznov, R. Merkle, E.A. Kotomin, J. Maier, Interdependence of Oxygenation and Hydration in Mixed-Conducting (Ba, Sr)FeO$_{3-\delta}$ Perovskites Studied by Density Functional Theory. J. Phys. Chem. C **124**(22), 11780–11789 (2020). https://doi.org/10.1021/acs.jpcc.0c01924

119. W.T. Hong, K.A. Stoerzinger, Y.-L. Lee, L. Giordano, A. Grimaud, A.M. Johnson, J. Hwang, E.J. Crumlin, W. Yang, Y. Shao-Horn, Charge-transfer-energy-dependent oxygen evolution reaction mechanisms for perovskite oxides. Energy Environ. Sci. **10**(10), 2190–2200 (2017). https://doi.org/10.1039/C7EE02052J

120. Y.-L. Lee, J. Kleis, J. Rossmeisl, Y. Shao-Horn, D. Morgan, Prediction of solid oxide fuel cell cathode activity with first-principles descriptors. Energy Environ. Sci. **4**(10), 3966–3970 (2011). https://doi.org/10.1039/C1EE02032C

121. M.W. Allen, S.M. Durbin, Influence of oxygen vacancies on Schottky contacts to ZnO. Appl. Phys. Lett. **92**, 122110 (2008). https://doi.org/10.1063/1.2894568

122. P. Wendel, S. Periyannan, W. Jaegermann, A. Klein, Polarization dependence of ZnO Schottky barriers revealed by photoelectron spectroscopy. Phys. Rev. Mater. **4**(8), 084604 (2020). https://doi.org/10.1103/PhysRevMaterials.4.084604

123. T. Takenaka, K.-I. Maruyama, K. Sakata, (Bi$_{1/2}$Na$_{1/2}$)TiO$_3$-BaTiO$_3$ System for Lead-Free Piezoelectric Ceramics. Jpn. J. Appl. Phys. **30**(9S), 2236 (1991). https://doi.org/10.1143/JJAP.30.2236

124. K. Reichmann, A. Feteira, M. Li, Bismuth Sodium Titanate Based Materials for Piezoelectric Actuators. Materials **8**(12) (2015). https://doi.org/10.3390/ma8125469

125. P.C. Bowes, G.H. Ryu, J.N. Baker, E.C. Dickey, D.L. Irving, Fermi level pinning in Co-doped BaTiO$_3$: Part II. Defect

chemistry models. J. Am. Ceram. Soc. **104**(11), 5859–5872 (2021). https://doi.org/10.1111/jace.17938

126. G.H. Ryu, P.C. Bowes, J.R. McGarrahan, D.L. Irving, E.C. Dickey, Fermi level pinning in Co-doped BaTiO$_3$: Part I. DC and AC electrical conductivities and degradation behavior. J. Am. Ceram. Soc. **105**(1), 292–298 (2022). https://doi.org/10.1111/jace.18042

127. B.A. Wechsler, M.B. Klein, Thermodynamic point defect model of barium titanate and application to the photorefractive effect. J. Opt. Soc. Am. B **5**, 1711 (1988). https://doi.org/10.1364/JOSAB.5.001711

128. H.-J. Hagemann, D. Hennings, Reversible Weight Change of Acceptor-Doped BaTiO$_3$. J. Am. Ceram. Soc. **64**(10), 590–594 (1981). https://doi.org/10.1111/j.1151-2916.1981.tb10223.x

129. P. Günter, J.-P. Huignard (eds.), *Photorefractive Materials and Their Applications 2: Materials* (Springer, New York 2007). https://doi.org/10.1007/BFb0120157

130. I. Denk, W. Münch, J. Maier, Partial conductivities in SrTiO$_3$: Bulk polarization experiments, oxygen concentration cell measurements, and defect-chemical modeling. J. Am. Ceram. Soc. **78**(12), 3265–3272 (1995). https://doi.org/10.1111/j.1151-2916.1995.tb07963.x

131. D.M. Long, A. Klein, E.C. Dickey, Barrier formation at BaTi$_3$ interfaces with Ni and NiO. Appl. Surf. Sci. **466**, 472–476 (2019). https://doi.org/10.1016/j.apsusc.2018.10.040

132. K.N.S. Schuldt, H. Ding, J.-C. Jaud, J. Koruza, A. Klein, Influence of defects on the Schottky barrier height at BaTiO$_3$/RuO$_2$ interfaces. Phys. Stat. Sol. (A) **218**, 2100143 (2021). https://doi.org/10.1002/pssa.202100143

133. I. Suzuki, B. Huang, T. Omata, A. Klein, Fermi Energy Limitation at β-CuGaO$_2$ Interfaces Induced by Electrochemical Oxidation/Reduction of Cu. ACS Appl. Energy Mater. **3**(9), 9117–9125 (2020). https://doi.org/10.1021/acsaem.0c01493

134. P. Erhart, A. Klein, D. Åberg, B. Sadigh, Efficacy of the DFT+U formalism for modeling hole polarons in perovskite oxides. Phys. Rev. B **90**, 035204 (2014). https://doi.org/10.1103/PhysRevB.90.035204

135. W. Heywang, Semiconducting barium titanate. J. Mater. Sci. **6**(9), 1214–1224 (1971). https://doi.org/10.1007/BF00550094

136. P. Lunkenheimer, V. Bobnar, A.V. Pronin, A.I. Ritus, A.A. Volkov, A. Loidl, Origin of apparent colossal dielectric constants. Phys. Rev. B **66**(5), 052105 (2002). https://doi.org/10.1103/PhysRevB.66.052105

137. G. Gregori, R. Merkle, J. Maier, Ion conduction and redistribution at grain boundaries in oxide systems. Prog. Mater. Sci. **89**, 252–305 (2017). https://doi.org/10.1016/j.pmatsci.2017.04.009

138. J. Maier, Ionic conduction in space charge regions. Prog. Solid-State Chem. **23**, 171–263 (1995). https://doi.org/10.1016/0079-6786(95)00004-E

139. R.A. De Souza, M. Martin, Using $^{18}O/^{16}O$ exchange to probe an equilibrium space-charge layer at the surface of a crystalline oxide: method and application. Phys. Chem. Chem. Phys. **10**, 2356–2367 (2008). https://doi.org/10.1039/b719618k

140. N. Sata, K. Eberman, K. Eberl, J. Maier, Mesoscopic fast ion conduction in nanometre-scale planar heterostructures. Nature **408**(6815), 946–949 (2000). https://doi.org/10.1038/35050047

141. T. Baiatu, R. Waser, K.-H. Härdtl, dc Electrical Degradation of Perovskite-Type Titanates: III, A Model of the Mechanism. J. Am. Ceram. Soc. **73**(6), 1663–1673 (1990). https://doi.org/10.1111/j.1151-2916.1990.tb09811.x

142. S. Rodewald, N. Sakai, K. Yamaji, H. Yokokawa, J. Fleig, J. Maier, The Effect of the Oxygen Exchange at Electrodes on the High-Voltage Electrocoloration of Fe-Doped SrTiO$_3$ Single Crystals: A Combined SIMS and Microelectrode Impedance Study. J. Electroceram. **7**(2), 95–105 (2009). https://doi.org/10.1111/j.1551-2916.2009.03061.x

143. C. Nicollet, C. Toparli, G.F. Harrington, T. Defferriere, B. Yildiz, H.L. Tuller, Acidity of surface-infiltrated binary oxides as a sensitive descriptor of oxygen exchange kinetics in mixed conducting oxides. Nature Catal. **3**(11), 913–920 (2020). https://doi.org/10.1038/s41929-020-00520-x

144. C. Nicollet, H.L. Tuller, Perspective on the Relationship between the Acidity of Perovskite Oxides and Their Oxygen Surface Exchange Kinetics. Chem. Mater. **34**(3), 991–997 (2022). https://doi.org/10.1021/acs.chemmater.1c03140

145. Y.-M. Chiang, T. Takagi, Grain-Boundary Chemistry of Barium Titanate and Strontium Titanate: I, High-Temperature Equilibrium Space Charge. J. Am. Ceram. Soc. **73**(11), 3278–3285 (1990). https://doi.org/10.1111/j.1151-2916.1990.tb06450.x

146. P. Ágoston, K. Albe, Ab initio modeling of diffusion in indium oxide. Phys. Rev. B **81**(19), 195205 (2010). https://doi.org/10.1103/PhysRevB.81.195205

147. W. Rheinheimer, J.P. Parras, J.-H. Preusker, R.A. De Souza, M.J. Hoffmann, Grain growth in strontium titanate in electric fields: The impact of space-charge on the grain-boundary mobility. J. Am. Ceram. Soc. **102**(6), 3779–3790 (2019). https://doi.org/10.1111/jace.16217

148. K.S.N. Vikrant, W. Rheinheimer, R.E. García, Electrochemical drag effect on grain boundary motion in ionic ceramics. npj Comput. Mater. **6**(1), 165 (2020). https://doi.org/10.1038/s41524-020-00418-z

149. A. Bikowski, K. Ellmer, A comparative study of electronic and structural properties of polycrystalline and epitaxial magnetron-sputtered ZnO: Al and Zn$_{1-x}$Mg$_x$O: Al Films-Origin of the grain barrier traps. J. Appl. Phys. **114**(6), 063709 (2013). https://doi.org/10.1063/1.4817376

150. F. Greuter, G. Blatter, Electrical properties of grain boundaries in polycrystalline compound semiconductors. Semicond. Sci. Technol. **5**(2), 111–117 (1990). https://doi.org/10.1088/0268-1242/5/2/001

151. J.Y.W. Seto, The electrical properties of polycrystalline silicon films. J. Appl. Phys. **46**(12), 5247–5254 (1975). https://doi.org/10.1063/1.321593

152. W. Mönch, *Semiconductor Surfaces and Interfaces* (Springer, Heidelberg 1993). https://doi.org/10.1007/978-3-662-04459-9

153. M.A. Green, E.D. Dunlop, J. Hohl-Ebinger, M. Yoshita, N. Kopidakis, A.W.Y. Ho-Baillie, Solar cell efficiency tables (Version 55). Prog. Photovolt. Res. Appl. **28**(1), 3–15 (2020). https://doi.org/10.1002/pip.3228

154. A. Reinders, P. Verlinden, W. van Sark, A. Freundlich, *Photovolt. Solar Energy* (John Wiley & Sons, Chichester 2017). https://doi.org/10.1002/9781118927496

155. R. Kirchheim, Reducing grain boundary, dislocation line and vacancy formation energies by solute segregation: II. Experimental evidence and consequences. Acta Mater. **55**(15), 5139–5148 (2007). https://doi.org/10.1016/j.actamat.2007.05.033

156. R.A. De Souza, The formation of equilibrium space-charge zones at grain boundaries in the perovskite oxide SrTiO$_3$. Phys. Chem. Chem. Phys. **11**, 9939–9969 (2009). https://doi.org/10.1039/b904100a

157. H.L. Tuller, ZnO grain boundaries: electrical activity and diffusion. J. Electroceram. **4**, 33–40 (1999). https://doi.org/10.1023/A:1009917516517

158. D. Makovec, M. Drofenik, Microstructural Changes during the Reduction/Reoxidation Process in Donor-Doped BaTiO$_3$ Ceramics. J. Am. Ceram. Soc. **83**(10), 2593–2599 (2000). https://doi.org/10.1111/j.1151-2916.2000.tb01594.x

159. D. Kohl, Function and applications of gas sensors. J. Phys. D.: Appl. Phys. **34**(19), 125–149 (2001). https://doi.org/10.1088/0022-3727/34/19/201

160. K. Hauffe, The Application of the Theory of Semiconductors to Problems of Heterogeneous Catalysis. Adv. Catal. **7**, 213–257 (1955). https://doi.org/10.1016/S0360-0564(08)60528-3

161. F.F. Vol'kenshtein, Experiment and the electronic theory of catalysis. Russ. Chem. Rev. **35**(7), 537 (1966). https://doi.org/10.1070/rc1966v035n07abeh001494

162. R. Merkle, J. Maier, How Is Oxygen Incorporated into Oxides? A Comprehensive Kinetic Study of a Simple Solid-State Reaction with $SrTiO_3$ as a Model Material. Angew. Chem. Int. Ed. **47**, 3874–3894 (2008). https://doi.org/10.1002/anie.200700987

163. C. Körber, A. Wachau, P. Ágoston, K. Albe, A. Klein, Self-Limited Oxygen Exchange Kinetics at SnO_2 Surfaces. Phys. Chem. Chem. Phys. **13**, 3223–3226 (2011). https://doi.org/10.1039/C0CP01935F

164. T.J.M. Bayer, J.-J. Wang, J.J. Carter, A. Moballegh, J. Baker, D.L. Irving, E.C. Dickey, L.-Q. Chen, C.A. Randall, The relation of electrical conductivity profiles and modulus data using the example of STO: Fe single crystals: A path to improve the model of resistance degradation. Acta Mater. **117**, 252–261 (2016). https://doi.org/10.1016/j.actamat.2016.07.024

165. H.T. Langhammer, T. Müller, K.-H. Felgner, H.-P. Abicht, Crystal Structure and Related Properties of Manganese-Doped Barium Titanate Ceramics. J. Am. Ceram. Soc. **83**(3), 605–611 (2000). https://doi.org/10.1111/j.1151-2916.2000.tb01239.x

166. T. Takeda, Y. Yamaguchi, H. Watanabe, S. Tomiyoshi, H. Yamamoto, Crystal and Magnetic Structures of $Sr_2Fe_2O_5$. J. Phys. Soc. Jpn. **26**(5), 1320–1320 (1969). https://doi.org/10.1143/JPSJ.26.1320

167. P.C. Bowes, J.N. Baker, D.L. Irving, Site preference of Y and Mn in nonstoichiometric $BaTiO_3$ from first principles. Phys. Rev. Mater. **4**(8), 084601 (2020). https://doi.org/10.1103/PhysRevMaterials.4.084601

168. M.N. Rahaman, *Ceramic Processing and Sintering* (CRC Press, Boca Raton 2003). https://doi.org/10.1201/9781315274126

169. B. Malič, D. Kuščer, M. Vrabelj, J. Koruza, *Review of methods for powder-based processing*. In: Stojanovic, B.D. (ed.) Magnetic, Ferroelectric, and Multiferroic Metal Oxides, pp. 95–120. (Elsevier, 2018). https://doi.org/10.1016/B978-0-12-811180-2.00005-0

170. R. Vassen, X. Cao, F. Tietz, D. Basu, D. Stöver, Zirconates as New Materials for Thermal Barrier Coatings. J. Am. Ceram. Soc. **83**(8), 2023–2028 (2000). https://doi.org/10.1111/j.1151-2916.2000.tb01506.x

171. O. Clemens, P.R. Slater, Topochemical modifications of mixed metal oxide compounds by low-temperature fluorination routes. Rev. Inorg. Chem. **33**(2–3), 105 (2013). https://doi.org/10.1515/revic-2013-0002

172. E.E. McCabe, C. Greaves, Fluorine insertion reactions into pre-formed metal oxides. J. Fluorine Chem. **128**(4), 448–458 (2007). https://doi.org/10.1016/j.jfluchem.2006.11.008

173. S.-J.L. Kang, *Sintering: Densification, Grain Growth, and Microstructure* (Elsevier, Amsterdam, 2005)

174. F. Lemke, W. Rheinheimer, M.J. Hoffmann, Sintering and grain growth in $SrTiO_3$: impact of defects on kinetics. J. Ceram. Soc. Jpn. **124**(4), 346–353 (2016). https://doi.org/10.2109/jcersj2.15265

175. H. Yoshida, S. Hashimoto, T. Yamamoto, Dopant effect on grain boundary diffusivity in polycrystalline alumina. Acta Mater. **53**(2), 433–440 (2005). https://doi.org/10.1016/j.actamat.2004.09.038

176. T. Bak, J. Nowotny, K. Prince, M. Rekas, C.C. Sorrell, Grain Boundary Diffusion of Magnesium in Zirconia. J. Am. Ceram. Soc. **85**(9), 2244–2250 (2002). https://doi.org/10.1111/j.1151-2916.2002.tb00442.x

177. T. Horita, N. Sakai, T. Kawada, H. Yokokawa, M. Dokiya, Grain-Boundary Diffusion of Strontium in (La, Ca)CrO_3 Perovskite-Type Oxide by SIMS. J. Am. Ceram. Soc. **81**(2), 315–320 (1998). https://doi.org/10.1111/j.1151-2916.1998.tb02336.x

178. R.K. Koju, Y. Mishin, Atomistic study of grain-boundary segregation and grain-boundary diffusion in Al-Mg alloys. Acta Mater. **201**, 596–603 (2020). https://doi.org/10.1016/j.actamat.2020.10.029

179. G. Gottstein, L.S. Shvindlerman, *Grain Boundary Migration in Metals* (CRC Press, Boca Raton 2009). https://doi.org/10.1201/9781420054361

180. W. Rheinheimer, M. Bäurer, C.A. Handwerker, J.E. Blendell, M.J. Hoffmann, Growth of single crystalline seeds into polycrystalline strontium titanate: Anisotropy of the mobility, intrinsic drag effects and kinetic shape of grain boundaries. Acta Mater. **95**, 111–123 (2015). https://doi.org/10.1016/j.actamat.2015.05.019

181. W. Rheinheimer, M. Bäurer, M.J. Hoffmann, A reversible wetting transition in strontium titanate and its influence on grain growth and the grain boundary mobility. Acta Mater. **101**, 80–89 (2015). https://doi.org/10.1016/j.actamat.2015.08.069

182. W. Rheinheimer, M.J. Hoffmann, Grain growth in perovskites: What is the impact of boundary transitions? Curr. Opin. Solid State Mater. Sci. **20**(5), 286–298 (2016). https://doi.org/10.1016/j.cossms.2016.04.004

183. P.-L. Chen, I.-W. Chen, Grain Growth in CeO_2: Dopant Effects, Defect Mechanism, and Solute Drag. J. Am. Ceram. Soc. **79**(7), 1793–1800 (1996). https://doi.org/10.1111/j.1151-2916.1996.tb07997.x

184. K. Matsui, H. Yoshida, Y. Ikuhara, Review: microstructure-development mechanism during sintering in polycrystalline zirconia. Int. Mater. Rev. **63**(6), 375–406 (2018). https://doi.org/10.1080/09506608.2017.1402424

185. P.-L. Chen, I.W. Chen, Grain Boundary Mobility in Y_2O_3: Defect Mechanism and Dopant Effects. J. Am. Ceram. Soc. **79**(7), 1801–1809 (1996). https://doi.org/10.1111/j.1151-2916.1996.tb07998.x

186. M. Kindelmann, K. Ran, W. Rheinheimer, K. Morita, J. Mayer, M. Bram, O. Guillon, Segregation-controlled densification and grain growth in rare earth-doped Y_2O_3. J. Am. Ceram. Soc. **104**(10), 4946–4959 (2021). https://doi.org/10.1111/jace.17907

187. M.N. Rahaman, R. Manalert, Grain boundary mobility of $BaTiO_3$ doped with aliovalent cations. J. Eur. Ceram. Soc. **18**(8), 1063–1071 (1998). https://doi.org/10.1016/S0955-2219(97)00215-X

188. C.A. Randall, A. Kelnberger, G.Y. Yang, R.E. Eitel, T.R. Shrout, High Strain Piezoelectric Multilayer Actuators-A Material Science and Engineering Challenge. J. Electroceram. **14**(3), 177–191 (2005). https://doi.org/10.1007/s10832-005-0956-5

189. B. Huang, P. Erhart, T. Yang, A. Klein, Electrostatic boundary conditions and (electro)chemical interface stability. Adv. Mater. Interfaces **10**(21), 2300332 (2023). https://doi.org/10.1002/admi.202300332